



University of Mohamed Kheider of Biskra
Exact Sciences and Sciences of Nature and Life
Matter Sciences

Final Dissertation in Master

Matter Sciences

Physics

Energy Physics and Renewable Energies

Ref :

Presented by:

Labed Madani

Numerical Simulation of InAs/GaAs Quantum well and Quantum dots solar cells

Jury:

Boumaraf Rami	M.C. « B »	Med Khider University- Biskra	President
Meftah Afak	Professor	Med Khider University- Biskra	Supervisor
Nouredine Sengouga	Professor	Med Khider University- Biskra	Examiner

Academic Year: **2018/2019**

Acknowledgement

*First, I would like to thank my advisor Pr. **Meftah Afak** for his valuable guidance and support during my dissertation and I am benefited a lot from her profound knowledge.*

It was a very nice experience to work with her.

*Also, I would like to thank Pr. **Noureddine Sengouga** for encourages me every time.*

*I would also like to thank **Labed Mohamed** and **Mehiri Fateh**, Who helped me in the basics of Silvaco.*

I also thank my family and my friends

(Ayoub, abdeljalil, kamel, mohyeddine, Fathi, hocine, fares, saleh, samih, Nadir, omar, youcef, fatih, messaoud, hasni, okba Benkhatta, Hamoudi, mohamed, youcef benbraïka, hichem mechehoud, sofiane, Ali, Kouider, abdelhak, ...).

Without forgetting to thank all my teachers without exception (A. Zerarka, M. Amjad, A. Chala, A. Ouahab, A. Ataf, T. Tibermacine, R. Boumaraf ... etc.).

I would not forget to thank the members of the jury, Dr. R. Boumaraf and Pr. N. Sengouga who have kindly accepted to read and examine our work,

Dedication

I dedicate this work to the best parents "Labad Miloud" and "Labad Zahia".

To my brother "Labad Islem".

ملخص:

في هذه المذكرة تمت دراسة خلية شمسية كمومية (InAs/GaAs). أولا في حالة الأبار الكمومية وثانيا في حالة النقاط الكمومية.

في حالة الأبار الكمومية، استعملنا MATLAB لتطوير برنامجنا الخاص لحل نموذج جر-انتشار مع نموذج شرودنغر- بواسون. قدمت الخلية الشمسية بالأبار الكمومية مردود 18.52% بالمقارنة ب 16.78% في حالة الخلية الشمسية الكلاسيكية.

تمت دراسة خلية شمسية بالنقاط الكمومية (InAs/GaAs) باستخدام برنامج محاكاة يدعى Silvaco Atlas. وتنقسم الدراسة الى قسمين: حالة مثالية وحقيقية. تمت دراسة تأثير عدد طبقات النقاط الكمومية وتأثير تطعيم النقاط الكمومية على الخصائص الكهربائية للخلية الشمسية بالنقاط الكمومية. تم الحصول على أعلى مردود والذي وصل الى 43.05 % في الحالة المثالية. في حين أنه قد وجد تجريبا مردود 9.1% مع الأخذ في عين الاعتبار وجود فخاخ للإلكترونات وذيول العصابات، تمكنا من الحصول على كفاءة تقدر ب 9.4% والتي تتفق مع النتيجة التجريبية. بالإضافة الى ذلك, كان من الممكن تحسين مردود الخلية الى 11.29% عن طريق تحسين عدد الطبقات و تطعيم النقاط الكمومية الى طبقتين و $1 \times 10^{19} cm^{-3}$ على التوالي .

Abstract

In this dissertation InAs/GaAs quantum solar cells is studied. First with a quantum well conception (QWSCs) and secondly with quantum dots (QDSCs).

For the InAs/GaAs QW, we used MATLAB to develop our own program to solve consistently the classical drift-diffusion model with Schrödinger-Poisson model. The QWSC provided a cell efficiency of 18.52% compared with 16.78% for the classical one.

The InAs/GaAs QDSC was studied using Silvaco Atlas simulator. The study is divided into two parts: ideal and real case. The effects of the number of quantum dots (QDs) layers and the doping of QDs on electrical properties of QDSC are investigated. A highest efficiency of 43.05 % was obtained in the ideal case. However experimental works have reported a conversion efficiency of 9.1%. Taking into account the presence of discrete electron traps and valence band tail, we were able to obtain a cell efficiency of 9.4% in agreement with experimental reports. In addition, it was possible to improve the cell efficiency to 11.29% by optimizing the number and the doping of QDs layers, to 2-layers and $1 \times 10^{19} \text{ cm}^{-3}$, respectively.

Table of contents

Acknowledgement	ii
Dedication	iii
ملخص	iv
Abstract	v
Table of contents	vi
Introduction	1
References	4
Chapter 1 : MQW solar cell principal and 1D simulation by MATLAB	5
1.1 Introduction.....	6
1.2 Quantum Well materials	7
1.2.1 Epitaxial growth of Quantum Well (QW)	7
1.2.2 Quantum-confined structures.....	8
1.3 Structure of Quantum Well solar cell.....	10
1.4 Modeling and simulation of QW solar cell	10
1.4.1 Classical Drift-Diffusion model	11
1.4.2 Quantum model	17
1.5 Application for InAs/GaAs p-i-n MQWSC	22
1.6 Conclusion	28
References	29
Chapter 2 : Numerical Modeling of Quantum dots solar cell by Silvaco-Atlas	30
2.1 Introduction.....	31
2.2 Researches and development of QDSCs	32
2.3 Physical mechanism of QDs solar cell.....	37
2.3.1 QDSC with intermediate band.....	38
2.3.2 QDSCs with multiple exciton generation.....	39
2.4 Structure of QDSC.....	40
2.5 Simulation setup in Silvaco Atlas.....	41
2.5.1 Introduction.....	41
2.5.2 Simulation steps for standard solar cell	48

2.5.3 Simulation of QDSC	50
References:.....	56
Chapter 3 : results and discussion	58
3.1 Introduction.....	59
3.2 Ideal QDs solar cell	59
3.2.1 Effect of number of quantum dots layers	61
3.2.2 Effect of doping QD layers.....	62
3.3 Real InAs/GaAs QDs solar cell.....	63
3.4 Optimization of the InAs/GaAs QDSC.....	70
3.4.1 Effect of doping QDs on the real J-V characteristic.....	70
3.4.2 Effect of using GaP layers in intrinsic region	71
3.4.3 Effect of number of QDs layers	72
3.5 Conclusion	75
References.....	76
Conclusion	78

Introduction

Self-assembled nanostructures are one of the most interesting topics in the last decade. Many exceptional properties can be obtained by downscaling the dimension of semiconductor to nanometer scale. The behavior of these nanomaterials is very different from the conventional one. Among of the most important property is the quantum effect which gives quantified energy levels. The electrical and optical properties of this type of materials can be engineered through controlling the material dimension and morphology. Over the last 20 years, many nanomaterials have been developed, including quantum well, quantum wire and quantum dots. The difference between these types is the number of the confined directions. The quantum dots (QDs) is defined as a nanostructure with a smaller sizes, in three dimensions, than the De-Broglie exciton wavelength [1]. QDs have been proposed as one of the most promising candidates for a wide range of applications [2] among which the solar cells field offers a potential interest with new concepts as the intermediate band and multi-exciton generation concepts [3]. The upper theoretical limit of the QDs based solar cell efficiency, calculated by what is called detailed balance limit, is more than 87% under concentrated sunlight [4]. Compared with the maximum efficiency of 30 % offered by single junction solar cell [5] this fact prompted researchers to focus further studies on Quantum dot Solar Cells (QDSCs).

The basic conception of a QDSC is a p-i-n structure in which the QDs are implanted in the intrinsic region. Among the available materials, InAs/GaAs QDs have been proposed to provide enhanced short-circuit current J_{sc} compared with the classical GaAs p-i-n solar cells [6]. However this enhancement go together with a reduction in the open circuit voltage V_{oc} . To avoid a significant decrease in V_{oc} and improve further the InAs/GaAs QDSC efficiency, several conception methods have been suggested. Among them the use of GaP strain-balancing layers in intrinsic region [7] [8]. Also doping the QDs helps to neutralize the electron traps, and then reduce the non-radiative recombination process [9]. Actually, the highest reported conversion efficiency of InAs/GaAs QDSC has reached 19.4 %, which is under two-sun illumination [10]. QDSC has not yet reached the expected efficiency and the main reason is due to further defects related to the QDs implantation. Therefore, the main purpose of this dissertation is to clarify which types of defects resulting from the QD are responsible for the difference between the upper theoretical efficiency this type of solar cells and their actual efficiency.

Consequently, the dissertation is composed of three chapters with further an introduction and a conclusion. In the first chapter, InAs/GaAs quantum well solar cell is simulated. We used MATLAB to develop our own program to solve consistently the classical drift-diffusion model with the quantum Schrödinger-Poisson model. This, to get an idea on the numerical methods and steps for this type of solar cells. In the second chapter SILVACO-ATLAS is presented to explain how the structure conception of the InAs/GaAs quantum dots is carried out and the principal electrical outputs simulated. In the third chapter, we will simulate InAs/GaAs QDSC first in the ideal case and examine if the number of the QDs and doping have a significant effect in this case. Then the real case is reproduced by introducing many defect types and in this case it was found also that QDs layer number and doping can improve significantly the cell efficiency.

References

- [1] K. D. Sattler, Handbook of nanophysics: nanoelectronics and nanophotonics, CRC Press, 2010
- [2] V. Reshma, P. Mohanan, Quantum dots: Applications and safety consequences, Journal of Luminescence (2018).
- [3] A. Luque, A. Marti, A. J. Nozik, Solar cells based on quantum dots: multiple exciton generation and intermediate bands, MRS bulletin 32 (2007) 236-241.
- [4] A. Belghachi, Theoretical calculation of the efficiency limit of solar cells, in: solar cells-New Approaches and Reviews, IntechOpen, 2015.
- [5] W. Shockley, H. J. Queisser, Detailed balance limit of efficiency of P-N junction solar cells, Journal of applied physics 32 (1961) 510-519.
- [6] A. Tukiainen, J. Lyytikainen, T.Aho, E. Halonen, M. Raappana, F. Cappelluti, M. Guina, Comparaison of 'shallow 'and 'deep' junction architectures for MBE-grown InAs/GaAs quantum dot solar cell, in: 2018 IEEE 7th world conference on Photovoltaic Energy Conversion (WCPEC) (A Joint Conference of 45th IEEE PVSC, 28th PVSEC & 34th EU PVSEC), IEEE, pp. 2950-2952.
- [7] C. G. Bailey, D. V. Forbes, S. J. Polly, Z. S. Bittner, Y. Dai, C. Mackos, R. P. Raffaele, S. M. Hubbard, Open-Circuit Voltage improvement of InAs/GaAs quantum dots solar cells using reduced InAs coverage, IEEE, Journal of Photovoltaics 2 (2012), 269-275.
- [8] S. Hubbard, C. Cress, C. Bailey, R. Raffaele, S. Bailey, D. Wilt, Effect of strain compensation on quantum dot enhanced GaAs solar cells, Applied Physics Letters 92 (2008) 123512.
- [9] X. Yang, K. Wang, Y. Gu, H. Ni, X. Wang, Z. Wang, Improved efficiency of InAs/GaAs quantum dots solar cell by Si-doping , Solar Energy Materials and Solar cells 113 (2013) 144-147.
- [10] K. Tanabe, D. Guimard, D.Bordel, Y. Arakawa, high-efficiency quantum dot solar cell by metalorganic chemical vapor deposition, Applied Physics Letters 100 (2012) 193905.

Chapter 1

MQW solar cell principal and 1D simulation by MATLAB

1.1 Introduction

The quantum well solar cells (QWSCs) were introduced for the first time by Barnham and Duggan [1] who have suggested a p-i-n structure where the quantum wells are inside the intrinsic region as shown **Fig 1.1**.

Quantum well is nanostructure material in which the confinement effect is only in one dimension. The quantum size effect becomes important when the thickness of the confining layer becomes comparable with the de Broglie wavelength of electrons and holes [2]. The main idea of the concept is to extend the absorption range of a high band gap material via the insertion of thin layers of lower band gap material in the intrinsic absorber region of the single junction.

In the multi-quantum well concept as shown in **Fig 1.1**, the quantum wells are separated by thick region of high band gap material. The charge carriers generated in the quantum wells need to escape to the conduction band and valence band of bulk material via thermionic emission or tunneling effect [3]. This leads to an increase in short circuit current (J_{sc}) but the open circuit voltage (V_{oc}) has been found to be reduced compared to samples without quantum wells [4]. The efficiency of MQW solar cell calculated in detailed balance limit with four intermediate bound is 74.6 % [5], but in reality, the efficiency do not exceed 15 % in one sun illumination [6].

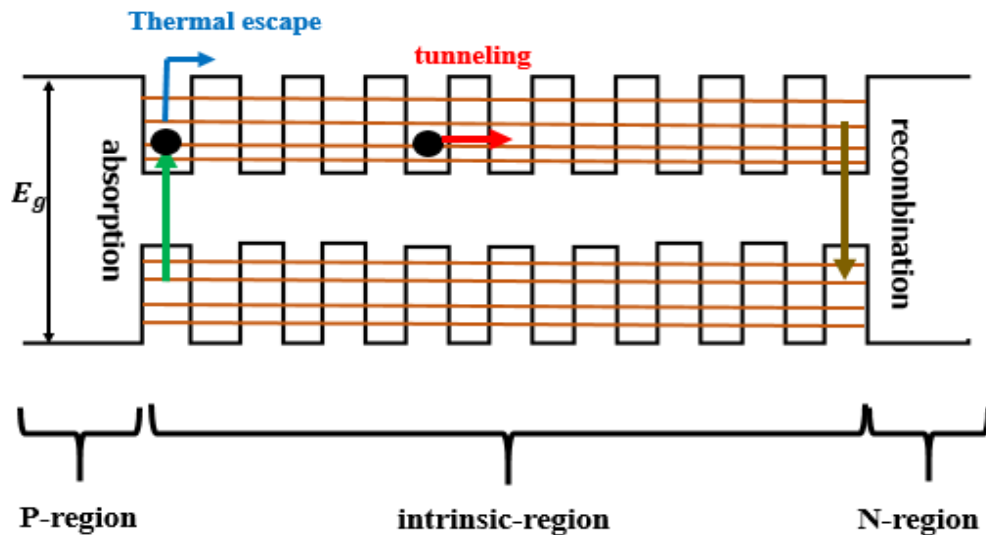


Fig 1.1 Schematic energy band diagram of multi-quantum well solar cell

1.2 Quantum Well materials

1.2.1 Epitaxial growth of Quantum Well (QW)

The art of bandgap engineering relies heavily on developments in the technology of crystal growth, exactly with development of epitaxial methods such as molecular beam epitaxy (MBE), and chemical beam epitaxy (CBE)... The basic principle of epitaxy is to grow thin layers of very high purity on top of bulk crystal called the substrate. The system is said to be lattice matched QW when the lattice constants of the epitaxial layer and the substrate are identical, for example growth $\text{Al}_x\text{Ga}_{1-x}\text{As}$ on GaAs ($\text{GaAs}/\text{Al}_x\text{Ga}_{1-x}\text{As}$ QW). Lattice matching reduces the number of dislocations in the epitaxial layer of quantum well system and other type of growth is strained where the substrate and the strained layers have different lattice constant (example InAs on GaAs). In order to avoid the build-up of misfit dislocation at interface in this type of growth, the strained layers need to be thinner enough. The layer can be physically strained to the point that its lattice constant becomes similar to that of the substrate [9]. This is more clarified in **Fig 1.2** and **Fig 1.3**.

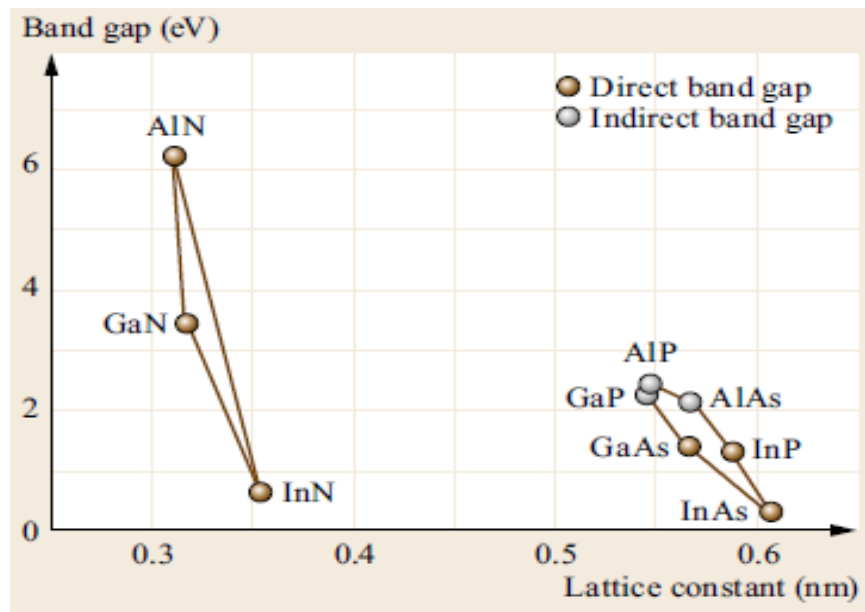


Fig 1.2 Room-temperature bandgap of a number of important optoelectronic III–V materials versus their lattice constant [8].

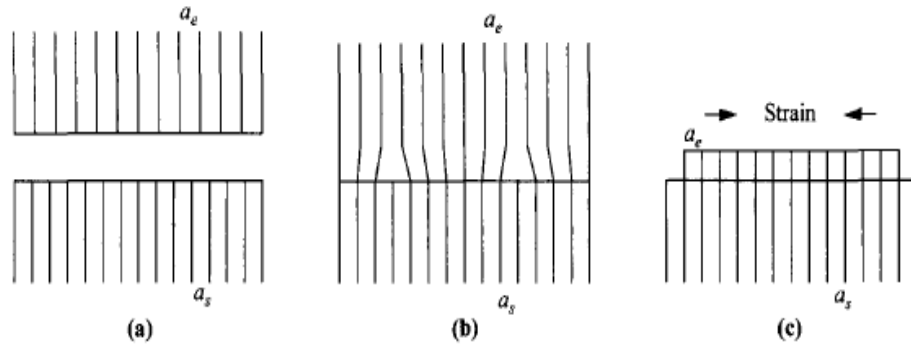


Fig 1.3: (a) Isolation lattice matched, (b) bulk strained layer with dislocation in interface, (c) thin strained layer without dislocation in interface [9].

1.2.2 Quantum-confined structures

A quantum-confined structure is one in which the motion of the electrons (and/or holes) is confined in one direction by potential barriers. Quantum size becomes important when the thickness of the layer becomes comparable to the de Broglie wavelength of the electrons or holes. The de Broglie wavelength depends on the effective mass of the particle m^* and temperature T :

$$\lambda_{de-Broglie} = \frac{h}{\sqrt{2m^*k_B T}} \quad (1-1)$$

For an electron and hole in InAs with an effective mass of $m_e^* = 0.023 m_0$ and $m_h^* = 0.41 m_0$ we find $\lambda_{de-Broglie(e)} = 50 \text{ nm}$ and $\lambda_{de-Broglie(h)} = 12 \text{ nm}$, respectively at 300K.

Thus, the length of the quantum well must be kept below the de-Broglie wavelength to observe the quantum confinement effects. Due to this, the motion of electrons and holes will be quantized in the growth direction, giving rise to a series of discrete energy levels as shown in **Fig 1.4 (a)**. The quantization of the motion in the growth direction has three main consequences: Firstly, the quantization energy shifts the effective band edge to higher energy; therefore, the bandgap tunability can be achieved without using alloys to control

the bandgap. This is desirable since alloys inevitably contain more defects than simple compound.

Secondly, the confinement keeps the electrons and holes closer together and hence increases the radiative recombination probability.

Finally, the density of state becomes independent of energy, in contrast to 3-D materials as shown in **Fig 1.4 (b)**.

The electronic states of QWs can be understood by solving the Schrödinger equation for electrons and holes. **Fig 1.4 (a)** illustrates the first two transitions in a typical QW; the threshold energy for these transitions is given by [8]:

$$\hbar\omega = E_g + E_{hn} + E_{en} \tag{1-2}$$

The lowest value is thus equal to $(E_g + E_{h1} + E_{e1})$, which shows that the optical bandgap is shifted by sum of the electron and hole confinement energies as shown in **Fig 1.4 (a)**.

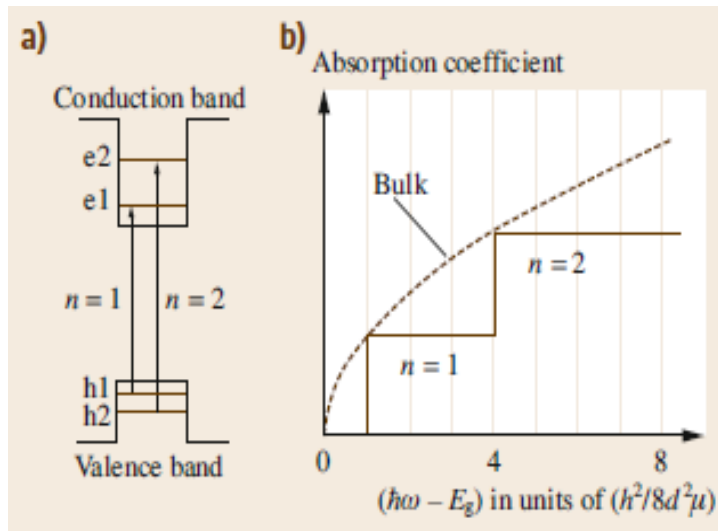


Fig 1.4 (a) Quantization energy levels and transition between confined states **(b)** absorption spectrum for bulk and quantum well materials [8].

1.3 Structure of Quantum Well solar cell

The solar cell is designed as a p-i-n structure where layers of lower bandgap is introduced into the intrinsic region, for example InAs used as QW and GaAs as matrix (or barrier) as shown in Fig 1.5.

The main idea of the quantum well in solar cell is to extend the absorption range of a GaAs material via the insertion of the thin layers of lower bandgap (InAs). The QW thickness must be less than de-Broglie Wavelength and this type of structure offers the possibility for reducing thermal dissipation loss through absorption photons with energy lower than bandgap of host material.

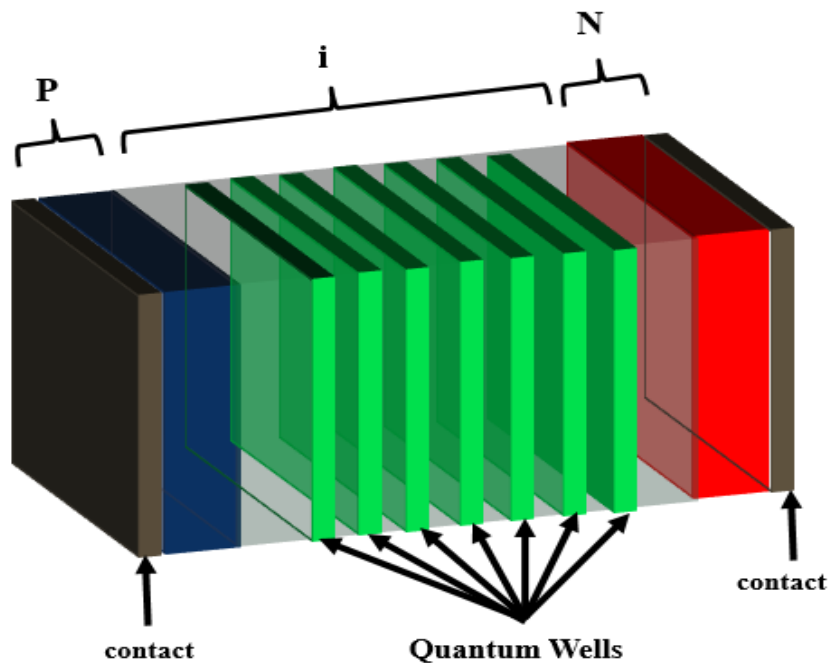


Fig 1.5 Structure of multi-quantum well solar cell

1.4 Modeling and simulation of QW solar cell

To simulate the MQWSCs two physical models are combined. The first one is the Drift-Diffusion model (DDM) which deals with classical regions. The solved system for DDM consists of Poisson and continuity equations. The second one is the tunneling-hopping quantum model (THQM) which describes the transport mechanism of quantum carriers

confined in wells. For the last one we solve consistently the Schrodinger and Poisson equations. **Fig 1.6** presents a simple illustration of the DDM for carriers at classical edges and the THQM for carriers confined in wells. Numerical method of each model is given in more details in next sections.

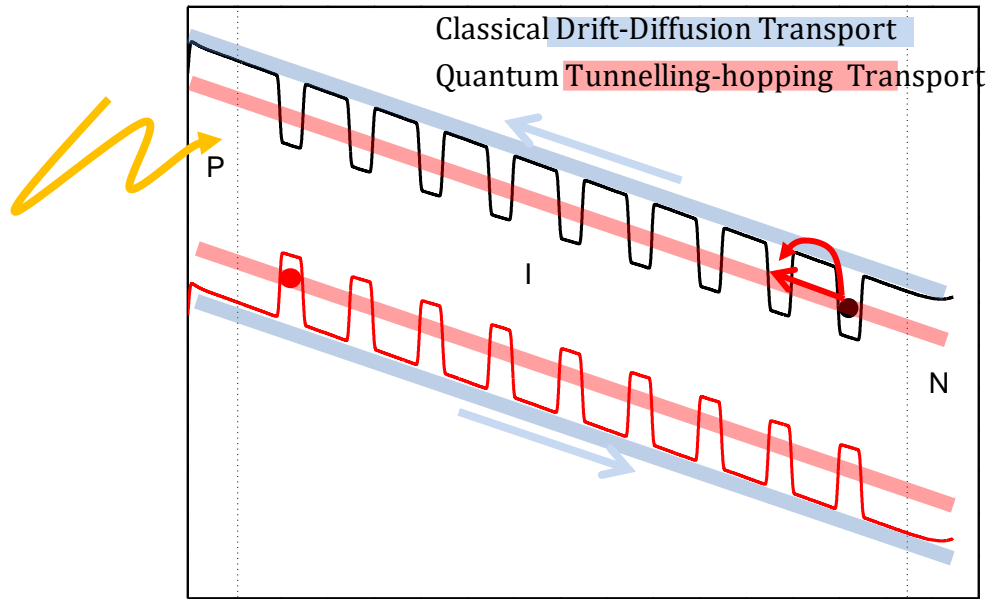


Fig 1.6 Transport Mechanism in QW solar cell

1.4.1 Classical Drift-Diffusion model

The classical DDM describes the static and dynamic behavior of carriers in semiconductors under external conditions, such as an applied field or an optical excitation, that cause deviation from the thermal-equilibrium condition. The basic equations can be classified in two groups; electrostatic equations, and continuity equations. by solving these equations, we can deduce the classical behavior of the solar cell. To solve these equations several numerical methods are available. In our study, we have chosen the Newton's iterative coupled method.

1.4.1.1 Basic equation of DDM

Poisson equation:

This equation relating charges to electric field (potential) for one dimension is given by [9]:

$$\frac{\partial^2 V}{\partial x^2} = -\frac{\partial \xi}{\partial x} = -\frac{\rho}{\varepsilon} = \frac{q(n-p+N_{AD}+p_t-n_t)}{\varepsilon} \quad (1-3)$$

$$N_{AD} = \begin{cases} +N_D, & \text{in } n \text{ region} \\ 0, & \text{in intrinsic region} \\ -N_A, & \text{in } p \text{ region} \end{cases} \quad (1-4)$$

ρ : Charge density (coulomb. cm^{-3})

n and p : The density of electrons and holes (cm^{-3})

N_{AD} : The density of doping (cm^{-3})

p_t and n_t : The density of traps states (cm^{-3})

ε : Dielectric constant of semiconductor. ($F \cdot cm^{-1}$)

This equation is commonly used in 1D solar cell or any other electronic device to calculate the potential and field profiles caused by a charge density (ρ) distribution.

Current-density Equations:

The most-common current conduction consists of the drift component, caused by the electric field, and the diffusion component, caused by the carrier-concentration non-uniformity distribution. The current-density equations are [9]:

$$J_n = q \mu_n n \xi + q D_n \frac{\partial n}{\partial x} \quad (1-5)$$

$$J_p = q \mu_p p \xi - q D_p \frac{\partial p}{\partial x} \quad (1-6)$$

$$J = J_n + J_p \quad (1-7)$$

Where J_n and J_p are the electron and hole current densities, respectively $\mu_{n,p}$ and $D_{n,p}$ are the mobility and the carrier diffusion constant.

Continuity Equations:

While the above current-density equations are for steady state conditions, the continuity equations deal with time-dependent phenomena such as low-level injection, generation and recombination.

Qualitatively, the net charge of carrier concentration is the difference between generation and recombination, plus the net current flow in and out of a given region. The continuity equations are then given by [9]:

$$\frac{\partial n}{\partial t} = G_n - U_R + \frac{1}{q} \frac{\partial J_n}{\partial x} \tag{1-8}$$

$$\frac{\partial p}{\partial t} = G_p - R_R - \frac{1}{q} \frac{\partial J_p}{\partial x} \tag{1-9}$$

Where G_n and G_p are the electron and hole generation rate ($cm^{-3}.s^{-1}$), respectively, caused by external influence such as the optical excitation. R_n and R_p are the recombination rate. For steady state $\frac{\partial n}{\partial t} = 0$ and $\frac{\partial p}{\partial t} = 0$.

1.4.1.2 Numerical simulation of DDM

To solve numerically the coupled partial differential equations (Poisson and continuity), the device structure should be divided into a number of nodes. This step is called a grid or mesh generation as shown in Fig 1.7.

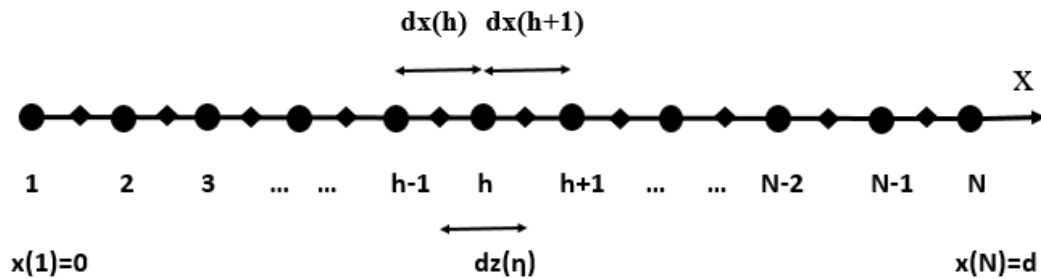


Fig 1.7 1D discretization of a solar cell.

The finite difference method is used for transform the differential equations to their discretized form. The principal variables n, p and V are defined in what is called main (principal) nodes. However, terms that contain the derivatives of the principal variables

(Electrical field, current) are defined at what is known by secondary (auxiliary) nodes. These are located between two main nodes.

The Poisson equation and the continuity equation in their discretized form according to finite difference method are then given by [10]:

$$\gamma_1(h)V(h-1) + \gamma_2(h)V(h) + \gamma_3(h)V(h+1) = -\frac{\rho(h)}{\varepsilon} \quad (1-10)$$

For Poisson equation where:

$$\gamma_1(h) = \frac{1}{\delta x(h)\delta z(\eta)}$$

$$\gamma_2(h) = \frac{1}{\delta z(\eta)} \left(\frac{1}{\delta x(h)} + \frac{1}{\delta x(h+1)} \right)$$

$$\gamma_3(h) = \frac{1}{\delta x(h+1)\delta z(\eta)}$$

For J_n and J_p we use Gummel approximation (more details concerning this approximation are given in [10]):

$$J_n(\eta+1) = \frac{q}{\delta x(h+1)} [\lambda_{n1}(\eta+1) n(h) + \lambda_{n2}(\eta+1) n(h+1)] \quad (1-11)$$

$$J_p(\eta+1) = \frac{q}{\delta x(h+1)} [\lambda_{p1}(\eta+1) p(h) + \lambda_{p2}(\eta+1) p(h+1)] \quad (1-12)$$

Where

$$\lambda_{n1}(\eta+1) = \mu_n \left(\frac{V(h)-V(h+1)}{1-\exp(\beta(\eta+1))} \right), \lambda_{n2}(\eta+1) = \mu_n \left(\frac{V(h)-V(h+1)}{1-\exp(-\beta(\eta+1))} \right)$$

$$\lambda_{p1}(\eta+1) = \mu_p \left(\frac{V(h)-V(h+1)}{1-\exp(-\beta(\eta+1))} \right), \lambda_{p2}(\eta+1) = \mu_p \left(\frac{V(h)-V(h+1)}{1-\exp(\beta(\eta+1))} \right)$$

$$\beta(\eta+1) = \frac{q}{K_B T} [V(h) - V(h+1)];$$

By using the Gummel approximation for the current-density, we find the discretized form of continuity equations:

$$\begin{aligned} & \frac{1}{\delta z(\eta)} \left(-\frac{\lambda_{n1}(\eta)}{\delta x(h)} n(h-1) + \left(\frac{\lambda_{n1}(\eta+1)}{\delta x(h+1)} - \frac{\lambda_{n2}(\eta)}{\delta x(h)} \right) n(h) \right. \\ & \quad \left. + \frac{\lambda_{n2}(\eta+1)}{\delta x(h+1)} n(h+1) \right) \\ & = -G(h) + U_R(h) \end{aligned} \quad (1-13)$$

$$\begin{aligned} & \frac{1}{\delta z(\eta)} \left(-\frac{\lambda_{p1}(\eta)}{\delta x(h)} p(h-1) + \left(\frac{\lambda_{p1}(\eta+1)}{\delta x(h+1)} - \frac{\lambda_{p2}(\eta)}{\delta x(h)} \right) p(h) \right. \\ & \quad \left. + \frac{\lambda_{p2}(\eta+1)}{\delta x(h+1)} p(h+1) \right) \\ & = G(h) + U_R(h) \end{aligned} \quad (1-14)$$

With $h=2:N-1$

Where

$$G(h) = \sum_{\lambda} \alpha(\lambda) \Phi_o \exp(-\alpha(\lambda) x(h)) \quad (1-15)$$

$$U_R(h) = \sum_{k=1}^{k=M} \frac{n(h)p(h)-n_i^2}{\tau_p(k) \left[n(h)+n_i \exp\left(\frac{E_T(k)-E_{Fi}}{K_B T}\right) \right] + \tau_n(k) \left[p(h)+n_i \exp\left(\frac{E_{Fi}-E_T(k)}{K_B T}\right) \right]} \quad (1-16)$$

Where M is the number of traps.

The full set of the discretized system is then written as:

$$F^V(h) = \gamma_1(h)V(h-1) + \gamma_2(h)V(h) + \gamma_3(h)V(h+1) + \frac{\rho(h)}{\varepsilon} = 0 \quad (1-17)$$

$$\begin{aligned} F^n(h) &= \frac{1}{\delta z(\eta)} \left(-\frac{\lambda_{n1}(\eta)}{\delta x(h)} n(h-1) + \left(\frac{\lambda_{n1}(\eta+1)}{\delta x(h+1)} - \frac{\lambda_{n2}(\eta)}{\delta x(h)} \right) n(h) + \frac{\lambda_{n2}(\eta+1)}{\delta x(h+1)} n(h+1) \right) \\ &+ G(h) - U_R(h) = 0 \end{aligned} \quad (1-18)$$

$$\begin{aligned} F^p(h) &= \frac{1}{\delta z(\eta)} \left(-\frac{\lambda_{p1}(\eta)}{\delta x(h)} p(h-1) + \left(\frac{\lambda_{p1}(\eta+1)}{\delta x(h+1)} - \frac{\lambda_{p2}(\eta)}{\delta x(h)} \right) p(h) + \frac{\lambda_{p2}(\eta+1)}{\delta x(h+1)} p(h+1) \right) \\ &- G(h) + U_R(h) = 0 \end{aligned} \quad (1-19)$$

Finally, a complete set of $3 \times (N - 1)$ equations is obtained that allows to calculate the values of $V(h)$, $n(h)$ and $p(h)$ ($h=2 \dots N - 1$) in each nodes.

Using these definitions, the complete set of non-linear algebraic equations can be written as

$$\begin{bmatrix} F(2) \\ F(3) \\ \\ F(h) \\ \\ \\ F(N - 1) \end{bmatrix} = 0; \text{ and } F(h) = \begin{bmatrix} F^V(h) \\ F^n(h) \\ F^p(h) \end{bmatrix} \quad (1-20)$$

$F(h)$ depends on $V(j)$, $n(j)$ and $p(j)$ where $j = h - 1, h, h + 1$.

The spatial discretization of the set of the three partial differential equations over N grid points results in a set of $3 \times (N - 2)$ nonlinear algebraic equations ($F(h) = 0$) with $3 \times (N - 2)$ unknowns.

Generally, iterative methods are used to solve systems of nonlinear algebraic equations. One of the most often used is the Newton method. After using the Taylor's series expansion to convert the nonlinear equation (1.17-18-19) into linear form, finally we found the following matrix-vector form:

$$A(h)\delta y(h - 1) + B(h)\delta y(h) + C(h)\delta y(h + 1) = F(h) \quad (1-21)$$

Where: $y(h) = \begin{bmatrix} p(h) \\ n(h) \\ V(h) \end{bmatrix}$ and $\delta y(h) = \begin{bmatrix} \delta p(h) \\ \delta n(h) \\ \delta V(h) \end{bmatrix}$

($h=2 \dots N - 1$)

To evaluate the matrix coefficients A, B, C and F let examine equation (1.21) in matrix form for three division points, $h-1$, h , and $h+1$:

$$\begin{bmatrix} a_{11}(h)a_{12}(h)a_{13}(h)b_{11}(h)b_{12}(h)b_{13}(h)c_{11}(h)c_{12}(h)c_{13}(h) \\ a_{21}(h)a_{22}(h)a_{23}(h)b_{21}(h)b_{22}(h)b_{23}(h)c_{21}(h)c_{22}(h)c_{23}(h) \\ a_{31}(h)a_{32}(h)a_{33}(h)b_{31}(h)b_{32}(h)b_{33}(h)c_{31}(h)c_{32}(h)c_{33}(h) \end{bmatrix} \begin{bmatrix} \delta p(h-1) \\ \delta n(h-1) \\ \delta V(h-1) \\ \delta p(h) \\ \delta n(h) \\ \delta V(h) \\ \delta p(h+1) \\ \delta n(h+1) \\ \delta V(h+1) \end{bmatrix} = \begin{bmatrix} f_{11}(h) \\ f_{12}(h) \\ f_{13}(h) \end{bmatrix}$$

Finally, we found the following Matrix-form

$$\begin{bmatrix} B(2) & C(2) & 0 & & & & & 0 \\ A(3) & B(3) & C(3) & & & & & 0 \\ 0 & A(4) & B(4) & C(4) & & & & \vdots \\ \vdots & & & & & & & \vdots \\ 0 & & A(h) & B(h) & C(h) & & & 0 \\ 0 & & & & & A(N-1) & B(N-1) & \vdots \\ 0 & & & & & & & \delta y(N-1) \end{bmatrix} \begin{bmatrix} \delta y(2) \\ \delta y(3) \\ \vdots \\ \delta y(h) \\ \vdots \\ \delta y(N-1) \end{bmatrix} = - \begin{bmatrix} F(2) \\ F(3) \\ \vdots \\ F(h) \\ \vdots \\ F(N-1) \end{bmatrix} \quad (1-22)$$

Newton's iteration principle requires that we have an initial guess or starting value to calculate the error state for the first iteration. The calculated error is then added to the initial value and the process is repeated until convergence is reached. For our MQWSC the DDM is used according steps described below to extract the J-V characteristic of the GaAs p-i-n. To improve the iterative processes we begin by calculate the J-V characteristic in dark. Each obtained solution in dark for the different applied voltages is used as initial guess when the light loop is added to extract finally the J-V characteristic under light.

1.4.2 Quantum model

1.4.2.1 Quantum transport in MQWSC

For MQWSC additional currents are available owing to confined carriers in wells; the thermionic emission current (hopping current) and the tunneling current.

The thermionic emission current is a majority carrier current and is always associated with a potential barrier. Note that the crucial parameter is the barrier height, not the shape of the barrier. Referring to **Fig 1.8**, for the thermionic emission to be the controlling mechanism the collision or the drift-diffusion processes within the barrier layer have to be negligible. Similarly, the barrier width has to be narrower than the mean free path, or in the case of a

triangular barrier, the slope of the barrier has to be reasonably steep such that $K_B T$ drop energy is within the mean free path. In addition, after the carriers are injected over the barrier, the diffusion current in that region must not be the limiting factor [9].

The second mechanism is the tunneling which is a quantum-mechanical phenomenon. From a classical point of view, carriers are completely confined by the potential walls. Only those carriers with excess energy higher than the barriers can escape, as in the case of thermionic emission discussed above. However, in quantum mechanics, an electron can be represented by its wavefunction.

The wavefunction does not terminate abruptly on a wall of finite potential height and it can penetrate into and through the barrier (**Fig 1.9**). The probability of electron tunneling through a barrier of finite height and width is thus not zero. To calculate the tunneling probability, the wavefunction Ψ has to be calculated from the solution of Schrödinger equation.

The tunneling current can be calculated from the product of the number of available carriers in the original (initial) region-A (**Fig. 1.9**), and the number of empty states in the destination region-B,

$$J_{Tun} = \frac{q m^*}{2 \pi^2 \hbar^3} \int F_A N_A \frac{|\psi_B|^2}{|\psi_A|^2} (1 - F_B) N_B dE \quad (1-23)$$

Where F_A, F_B, N_A, N_B and $\frac{|\psi_B|^2}{|\psi_A|^2}$ present the Fermi-Dirac distribution (in region A and B respectively), their corresponding densities of states and the tunneling probability respectively [9].

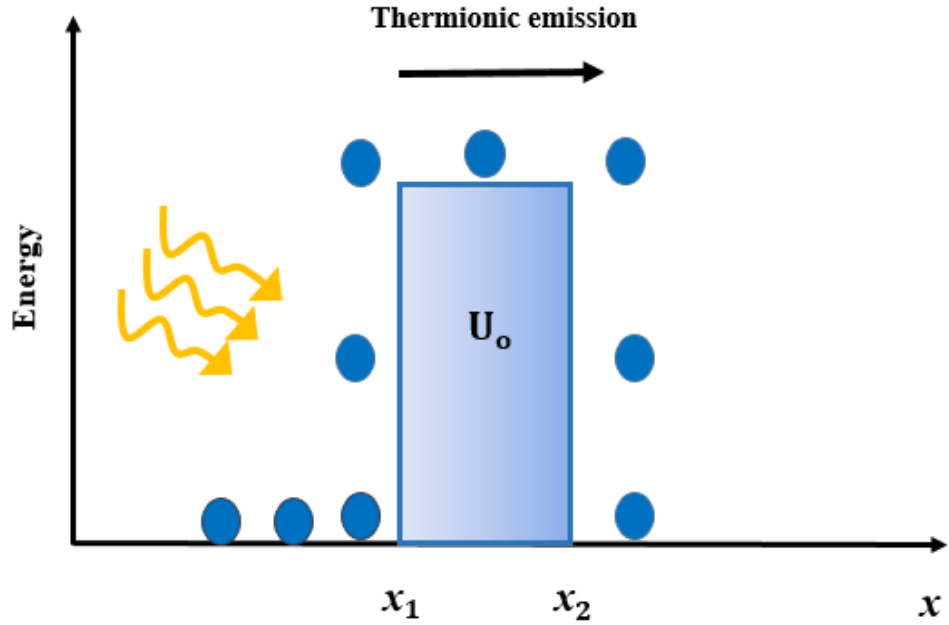


Fig 1.8 Energy-band diagram of thermionic emission of electrons over a barrier.

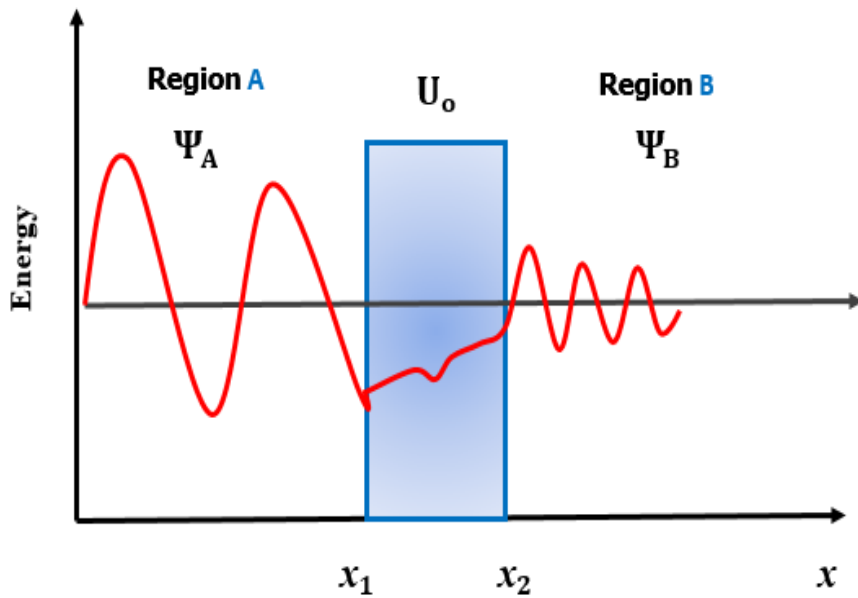


Fig 1.9 Electron wavefunction tunneling through a rectangular barrier.

1.4.2.2 Numerical simulation method for the quantum model

To simulate the quantum model in MQWSC, the Schrödinger equation must to be solved to calculate the eigenvalues (Energies) and eigenvectors (wavefunctions) of the confined carriers (electrons and holes). We have the pivotal idea championed by Dirac that column vectors (kets) and that differential operators correspond to matrix (bra-ket). The finite difference method (F.D.M) are used to transform the Hamiltonian operator to a matrix [11]:

$$\frac{\hbar^2}{2} \left[\frac{\partial}{\partial x} \left(\frac{1}{m_e^*} \frac{\partial \Psi_i}{\partial x} \right) \right] + E_c \Psi_i = E_i \Psi_i \quad (1-24)$$

$$\frac{\hbar^2}{2} \left[\frac{\partial}{\partial x} \left(\frac{1}{m_h^*} \frac{\partial \Psi_j}{\partial x} \right) \right] - E_v \Psi_j = E_j \Psi_j \quad (1-25)$$

Finally, we found the following form of the discretized equations:

$$a_P(h) \Psi(h) - a_E(h) \Psi(h+1) - a_W(h) \Psi(h-1) = E \Psi(h) \quad (1-26)$$

For electrons, where;

$$a_E(h) = -\frac{\hbar^2}{2} \frac{\frac{1}{m_e^*(h)} + \frac{1}{m_e^*(h+1)}}{2} \frac{1}{dx(h+1)dz(\eta)}$$

$$a_W(h) = -\frac{\hbar^2}{2} \frac{\frac{1}{m_e^*(h)} + \frac{1}{m_e^*(h-1)}}{2} \frac{1}{dx(h)dz(\eta)}$$

$$a_P(h) = a_E(h) + a_W(h) + E_c$$

Finally, equations (1-26) are writing on the form of eigenvalues problem:

$$\hat{H}|\Psi\rangle = E|\Psi\rangle \quad (1-27)$$

It is possible in MATLAB to solve Eq (1-27) and extract the eigenvalues E and the eigenvectors $|\Psi\rangle$ of \hat{H} . This by using the command $[\varphi, E] = \text{eig}(H)$ which generates two matrices. The first matrix φ has as its columns the eigenvectors $|\Psi\rangle$. The second matrix E is a diagonal matrix with Eigen values E_i corresponding to the eigenvectors $|\Psi_{E_i}\rangle$ placed along the central diagonal. We can use the command $E = \text{diag}(E)$ to covert this matrix into a column vector [11].

After finding the eigenstates and eigenvalues, it is possible now to calculate the quantum concentration of electrons and holes, according to the following relations [2]:

$$n_{QW} = 2 \frac{\sqrt{2 m_e^* K_B T}}{h} \sum_i |\Psi_i|^2 F_{-1/2} \left(-\frac{E_i - E_F}{K_B T} \right) \quad (1-28)$$

$$p_{QW} = 2 \frac{\sqrt{2 m_h^* K_B T}}{h} \sum_j |\Psi_j|^2 F_{-1/2} \left(-\frac{E_f - E_j}{K_B T} \right) \quad (1-29)$$

Where m_e^* and m_h^* are the electron and hole effective masses, E_f is the Fermi level, and $F_{-1/2}$ is the Fermi-Dirac integral of order $-1/2$.

These quantum concentrations in addition to the classical concentrations (calculated from DDM) are injected in Poisson equation as follows:

$$\frac{\partial^2(\epsilon V)}{\partial x^2} = -\rho = q(N_{AD} - p_{QW} - p_{class} + n_{QW} + n_{class}) \quad (1-30)$$

We note that the iterative process and the convergence test are applied to this equation after its discretization similarly to Poisson equation in DDM. This is done alternately with the Schrödinger equation. For the hopping and tunneling probability, we assume for simplicity that due to the availability of many photons with different energies, all the carries generated in quantum wells can escape. Then the quantum current can be calculated as follows:

$$J_{n,Quantum} = q \int \frac{\Delta n_{Quantum}}{\tau_n} dx \quad (1-31)$$

$$J_{p,Quantum} = q \int \frac{\Delta p_{Quantum}}{\tau_p} dx \quad (1-32)$$

$$J_{Quantum} = J_{n,Quantum} + J_{p,Quantum} \quad (1-33)$$

Finally, the complete flowchart of the algorithm used to extract the total J-V characteristic under light of the InAs/GaAs p-i-n MQWSC is shown in **Fig.1.10**.

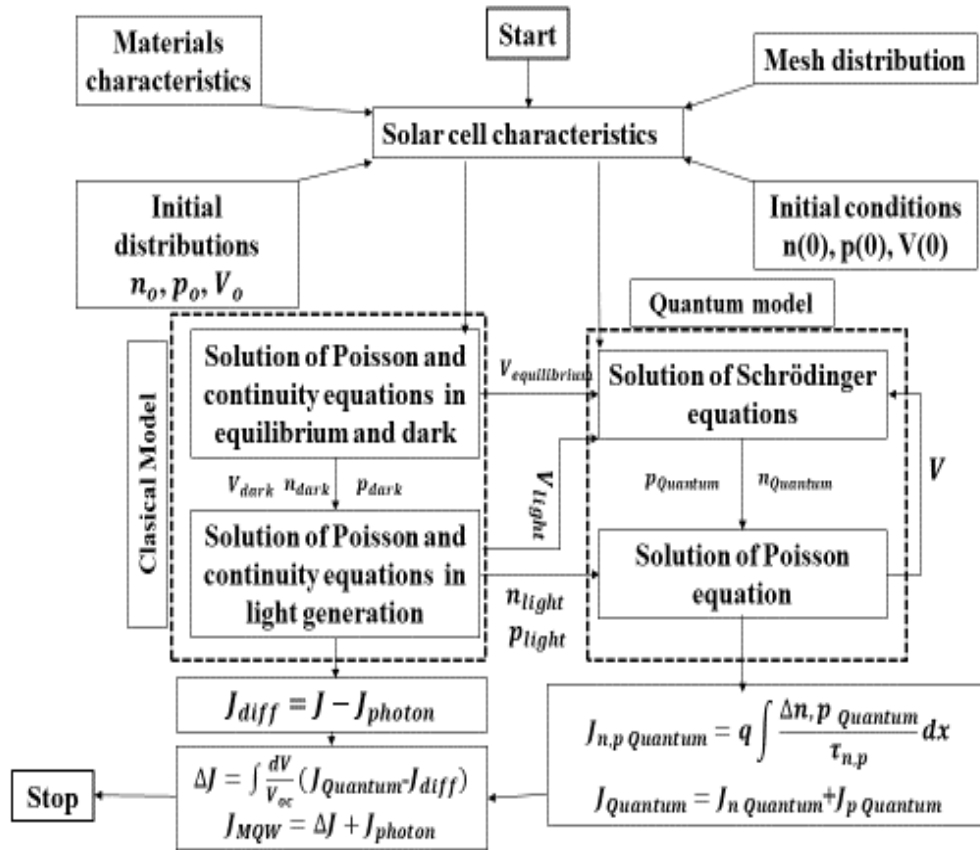


Fig 1.10 Flowchart of the algorithm of MQWSC.

1.5 Application for InAs/GaAs p-i-n MQWSC

Along this dissertation, we simulate InAs/GaAs multi-quantum well shown in Fig 1.11, nine quantum wells are used with 10-nm thickness and distance between two QW is 10-nm and all simulations were performed at room temperature using AM0 solar irradiance at intensity of one sun.

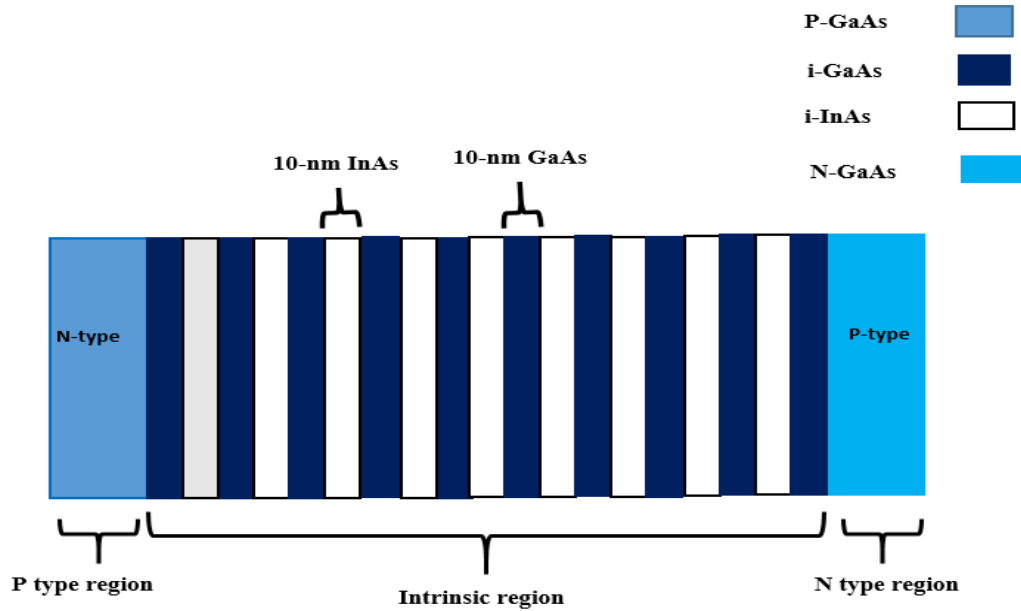


Fig 1.11 Structure of InAs/GaAs multi-quantum well solar cell.

The band diagram of this structure, Eigen energies calculated by MATLAB are shown in **Fig 1.12**. Quantum electrons and holes wavefunction and quantum concentration distribution calculated in equilibrium are presented, respectively, in **Fig 1.13** and **Fig.1.14**. From figure, we can see that, due the profile of the p-i-n energy diagram (the internal build in field) the electrons moved from the intrinsic region to the n-region as shown below, and holes from intrinsic to p-region.

It is known that by applying light to the solar cell an optical direct bias will be generated along the cell. As results the quantum concentrations distribution of electrons and holes change as if it was a direct bias applied. Hence, the electrons move from n-region to p-region and the holes from p-region to n-region as shown in **Fig 1.15**.

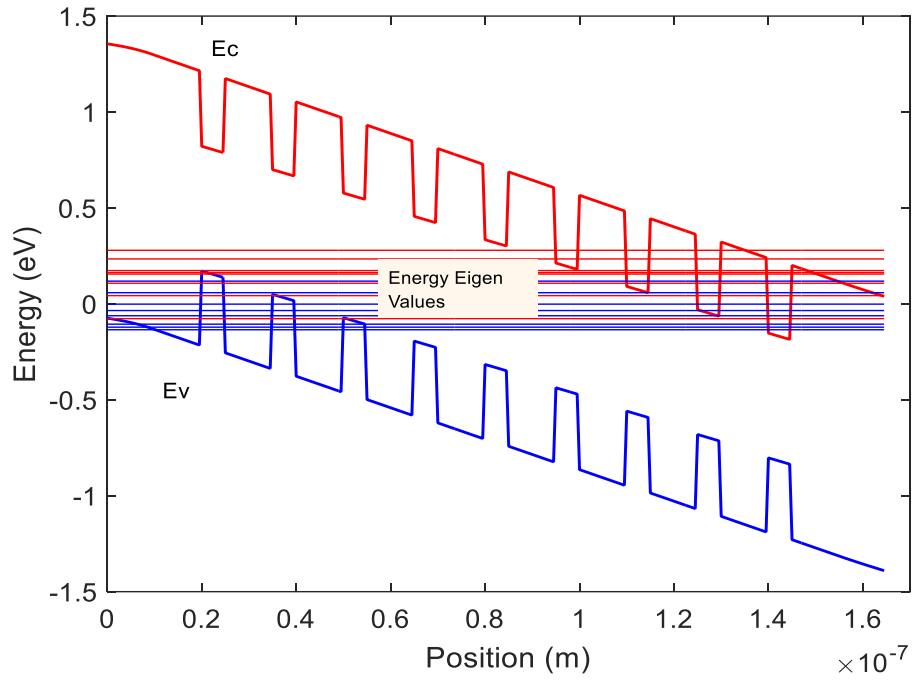


Fig 1.12 Simulated band diagram of InAs/GaAs MQWSC and its extracted Eigen energies.

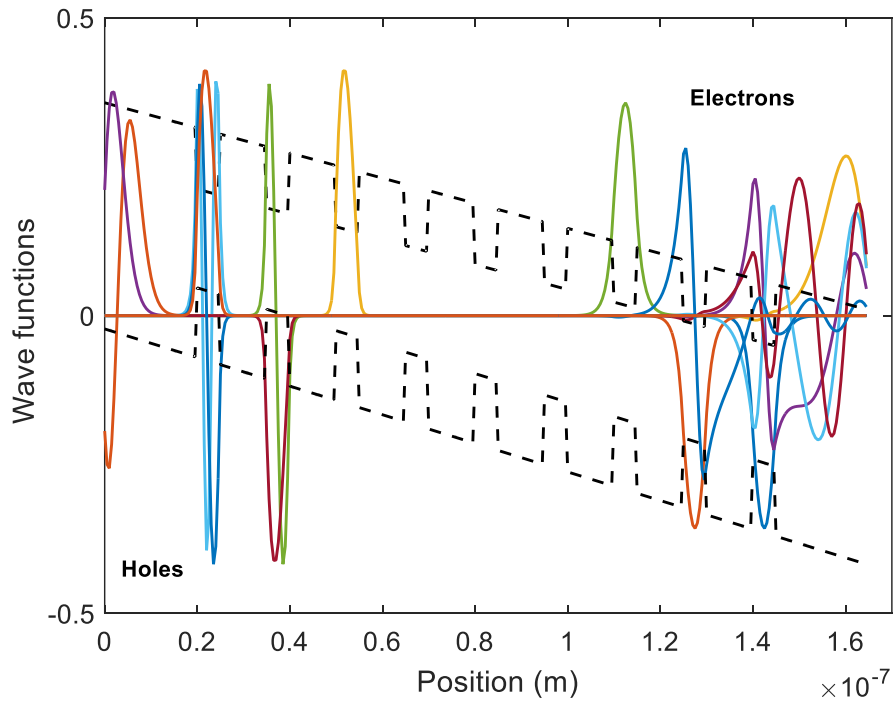


Fig 1.13 Wavefunctions distribution for electrons and holes.

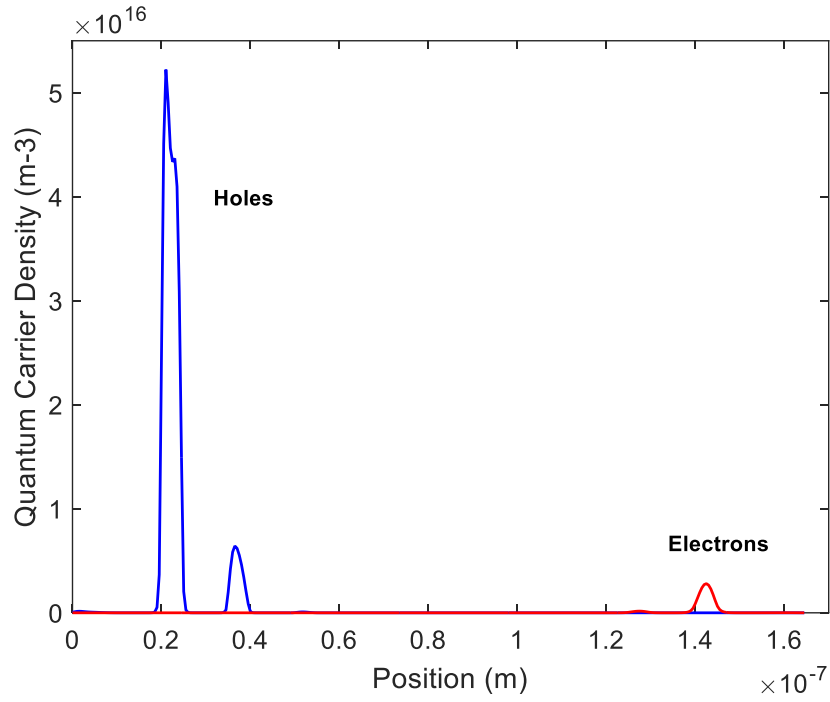


Fig 1.14 Quantum concentration distribution in equilibrium for electrons and holes.

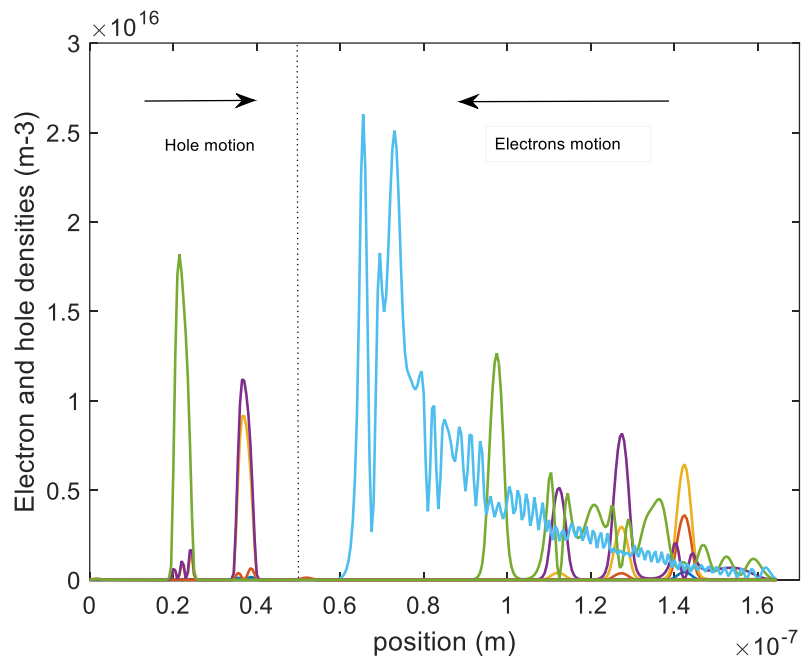


Fig 1.15 Quantum concentration distribution in light bias for electrons and holes.

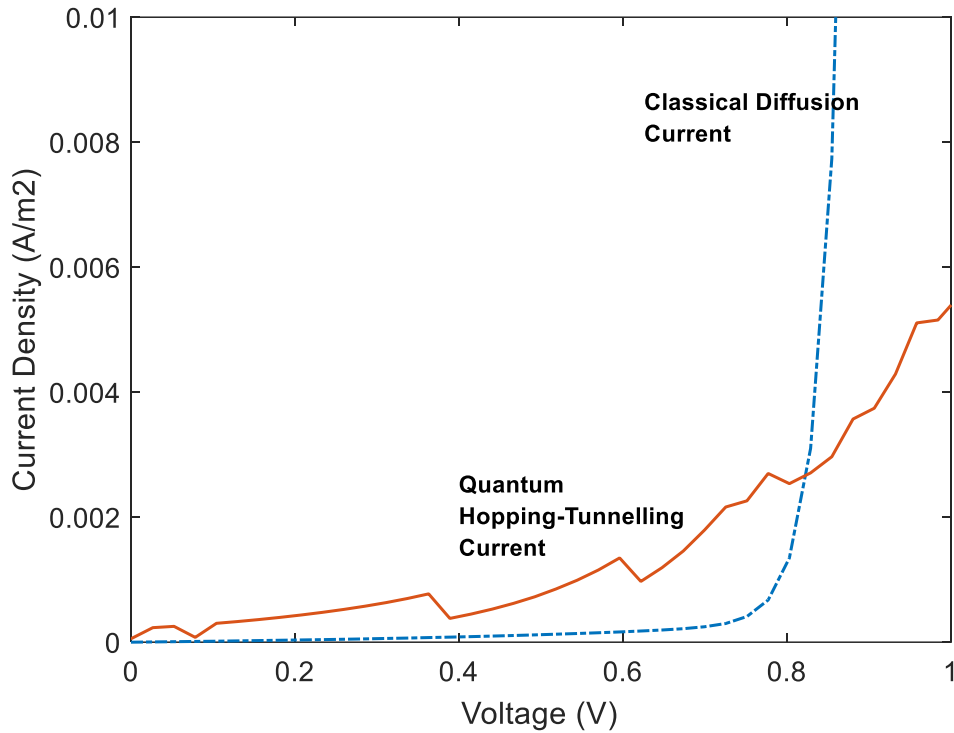


Fig 1.16 Quantum current of MQW solar cell and classical diffusion current of classical solar cell.

Fig 1.16 shows the simulated classical diffusion current and the quantum current densities. These two currents are comparable. The oscillating shape noticed in the quantum current density is produced by the wavefunction behavior.

Finally, the J-V characteristic under light is shown in **Fig 1.17** compared with the J-V of classical solar cell. The extracted electrical outputs are summarized in **Table 1**. We notice significant increase in J_{sc} and FF and the cell efficiency improves for 16.78 % to 18.52%. However V_{oc} does not change because in this simulation we have omitted recombination for carriers generated in QW (very low defect density and then SRH recombination can be neglected).

Therefore, the beneficial effect of QW is clear. The contribution of the quantum phenomena assisted by quantum carrier thermal emission and tunneling has notably improved the cell current density.

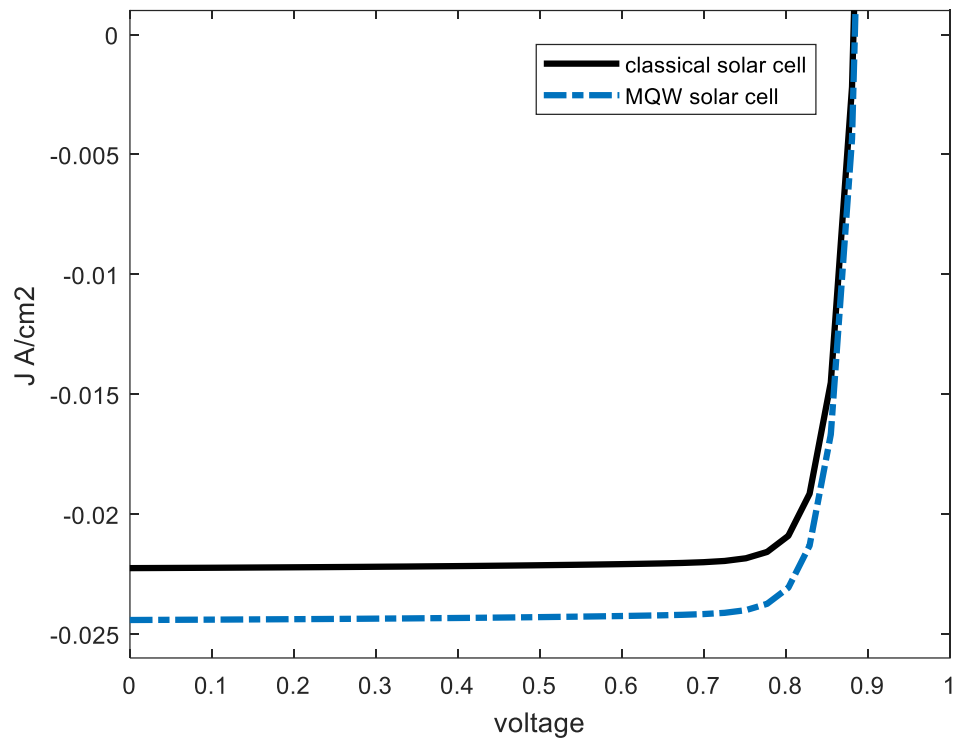


Fig 1.17 J-V characteristics of InAs/GaAs p-i-n MQWSC compared to the same classical solar cell.

Table 1 Comparison between GaAs/InAs p-i-n MQWSC and standard GaAs p-i-n SC.

GaAs p-i-n SC	J_{sc} (A/cm ²)	V_{oc} (V)	η (%)	FF (%)
Standard solar cell	0.0222	0.881	16.78	85.47
MQW solar cell	0.0244	0.881	18.52	86.20

1.6 Conclusion

In this chapter, we have presented the numerical models and method to simulate a 1D MQWSC in MATLAB. The numerical model consists of the classical DDM for classical carriers at the higher band gap edge while the quantum model deals with carriers confined in wells formed by lower band gap edge. The numerical method used in both models is Newton method and additional commands provided by MATLAB to extract the Eigen values of energies and wavefunctions in wells. Using MATLAB the total built program applied to a InAs/GaAs p-i-n MQWSC gives promising results especially concerning current density and fill factor. This leads to an increase of the cell efficiency to 18.52% compared to 16.78% of the classical GaAs p-i-n SC.

As far as future recommendations go, by considering the recombination model in QW, tunneling through traps and other models it is possible to improve the study and obtain results reflecting more the experimental measurements.

In addition, MQWSC open minds of designers to establish other modern conceptions to improve more the conversion efficiency, like as the quantum dot solar cell which will be presented in the next chapter using the well-known powerful “SILVACO ATLAS” simulator.

References

- [1] Barnham, I. Ballard, J. Connolly, N. Ekins-Daukes, B. Klufftinger, J. Nelson, C. Rohr, Quantum Well solar cell, *Physica E: Low-dimensional Systems and Nanostructures* 14 (2002), 27-35
- [2] Aritra Acharyya et al “Self-consistent solution of Schrödinger-Poisson equations in a reverse bias nano-scale p-n junction based on Si /Si_{0.4}Ge_{0.6}/Si quantum well, computer electron, 2014, DOI: 10.1007/s10825-014-0637-1.
- [3] J. R. Lang et al “Carrier escape mechanism dependence on barrier thickness and temperature in InGaN quantum well solar cells”, *Applied physics letters*, 2012 (101), DOI: 10.1063/1.4765068
- [4] Richard Corkish and Martin A. Green “RECOMBINATION OF CARRIERS QUANTUM WELL SOLAR CELLS”, *IEEE*, 1993 (93).
- [5] Tomohiro Nazawa et al “Detailed balance limit of the efficiency of multilevel intermediate band solar cells”, *Applied physics letters*, 2011 (98), 171108
- [6] Tatsuya Nakata et al “Thin-film multiple-quantum-well solar cells fabricated by epitaxial lift-off process”, *Japanese journal of applied Physics*, 2018 (57), 08RF03
- [7] U. Aeberhard, Simulation of nanostructure-based high-efficiency solar cells; challenges, existing approaches, and future directions, *IEEE Journal of Selected Topics in Quantum electronic* 19 (2013), 1-11.
- [8] S. Kasap, P. Capper “Handbook of Electronic and Photonic Materials”, chapter 40, springer, DOI 10.1007/978-3-319-48933-9_40.
- [9] S. M. SZE and KWOK K. NG “Physics of semiconductor devices”, chapter 1, 2007, Wiley and Sons.
- [10] ASA, User's Manual, version 4, April 2003.
- [11] R. Garcia, A. Zozulya, J. Stickney, MATLAB codes for teaching quantum physics: Part 1, arXiv preprint arXiv: 0704.1622 (2007).

Chapter 2

Numerical modeling of Quantum dots solar
cell by SILVACO-ATLAS

2.1 Introduction

The intermediate band and Multi-exciton generation solar cells are a photovoltaic concepts designed to give a performance exceeding that of a single gap solar cells. The basic principles behind its operation rely on synthesizing a semiconductor material with an electronic band located within the band gap and carrier recombination between bands should be much slower than the relaxation within the bands for capture and use photon less than the bandgap energy [2] or synthesizing a semiconductor with an intraband transitions equivalent to the bandgap of semiconductor for more benefit and use photon more than the bandgap energy [2].

Quantum dots (QDs) have been proposed as a way of both implementing the intermediate band concept and Multi exciton generation. QDs is a nanostructure whose sizes in three dimensions are all smaller than De Broglie wavelength of excitons and size between molecular and bulk forms of material. As a result, the moving space of electrons will become smaller than the De Broglie wavelength with the confinement effect of quantum dots, which is about tens of nanometers. The classic corpuscular property will no longer applies to the moving electrons. Instead, wave property will become the main character, which leads to a lot of quantum effects that benefit in designing and making use of quantum dot solar cell, such as size effect, resonant tunneling effect, multiple excitons effect and so on, for example the bandgap of QDs increases with the size decreasing and the energy levels in quantum dots are quantized due to quantum confinement effect in three dimensions [3].

As calculated result from Detailed Balance limit , the conversion efficiency of Quantum Dots solar cell is more than 87% under concentrated sunlight [4], comparing with maximum efficiency of single junction solar cell (30%) [5].

Many research results have been presented about different quantum dot solar cells (QDSCs) with different materials and structures. Up to now, the highest reported conversion efficiency of fabricated QDSCs has reached 19.4% which is under two-sun illumination [6] there are other attempts to understand the behavior of QDs and defects in this type of materials.

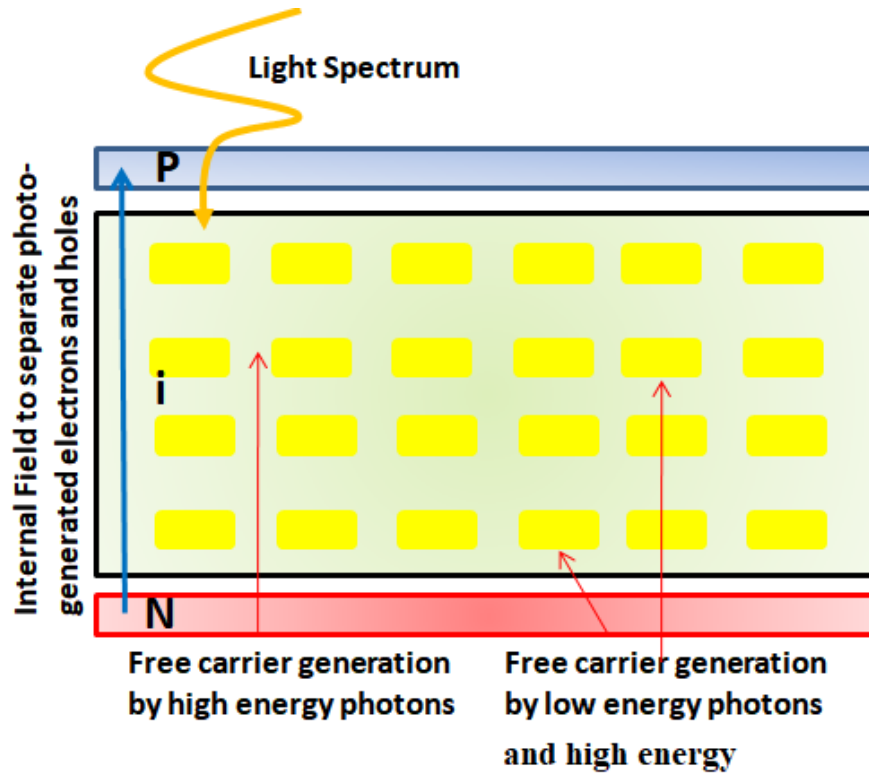


Fig 2.1 Structure of quantum dots solar cell

A simplified structure of a QDSC is presented in **Fig.2.1**. When the cell is subject to the light, photons of the higher energies are absorbed mainly by the basic matrix semiconductor of the *i* region which has the higher band gap energy. The quantum dot implanted in the *i* region absorb, in addition, lower energy photons. As results, an improve is expected in the current density while an effective voltage is established combined between the higher one related to the basic matrix and the lower of the QD regions. The conversion efficiency of the cell gets better if the increase in current exceeds the voltage drop.

2.2 Researches and development of QDSCs:

In 2007, Marti et al used molecular beam epitaxy for growth and compared between InAs/AlGaAs QDs solar cell with different number of Q.D layers, 10, 20 and 40 layers of Q.Ds and they found that [1]:

- The number of QDs layers plays an important role in the solar cell properties.

- The short circuit current does not always increase with more layers of Q.Ds and solar cell with 10 layers have the highest J_{sc} as shown in **Fig 2.2**.

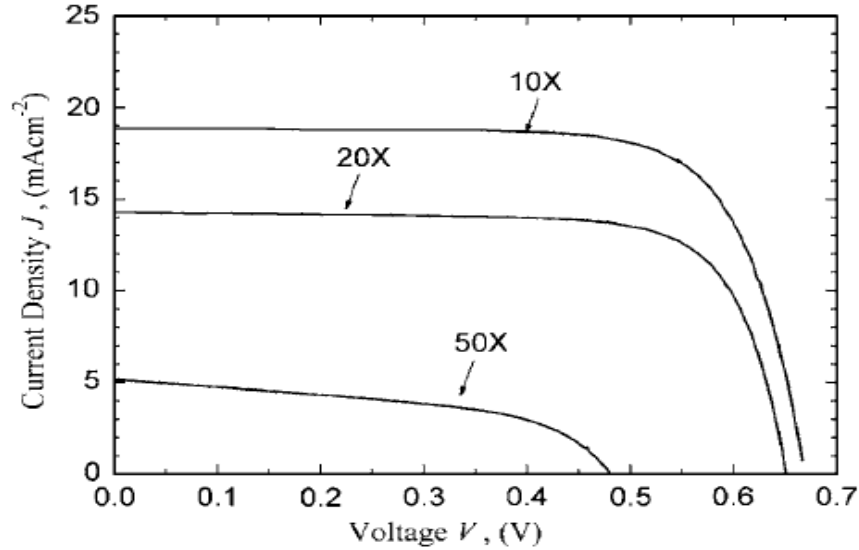


Fig 2.2 J-V curves of different layers of InAs QD solar cells [1].

The authors interpreted that by decrease in the minority carries lifetime and by strain-induced dislocation that propagate from QDs region to P emitter.

In the same year R. B. Laghumavarapu et al inserted GaP (Gallium Phosphate) layers into 3-layer InAs/GaAs quantum dot solar cell [7] [3]. They found an enhanced infrared spectral response of GaAs-based solar cells that incorporate type II GaSb quantum dots (QDs). These are formed using interfacial misfit array growth mode and the technique used for growth is the molecular beam epitaxy as show in **Fig 2.3** [7].

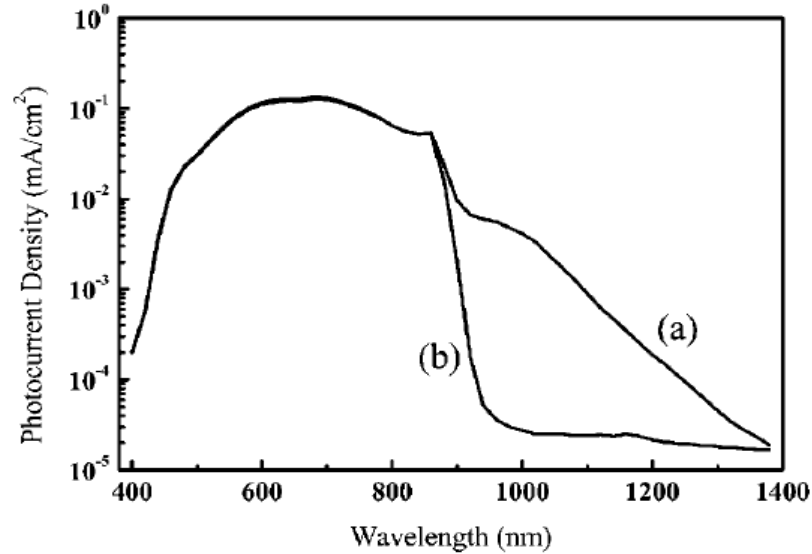


Fig 2.3 Spectral response of (a) solar cell with type-2 GaSb/GaAs quantum dot and (b) solar cell without type-2 GaSb/GaAs quantum dot [7].

In addition, the authors proved that the QDs type II is more efficient than type I, because the only one type of carrier is confined and therefore decrease the recombination in QDs.

In 2012, Bailey et al use a thin layer of GaP or GaAsP to compensate strain or at least to partially accommodate the compressive strain induced by InAs QDs sheets. The structure is illustrated in **Fig 2.4**. The most important result in their work is the improvement of the open-circuit voltage compared to the other QD solar cells and was found to be due to the reduction of non-radiative recombination resulting from a reduced density of larger defective QDs and effective strain management [8].

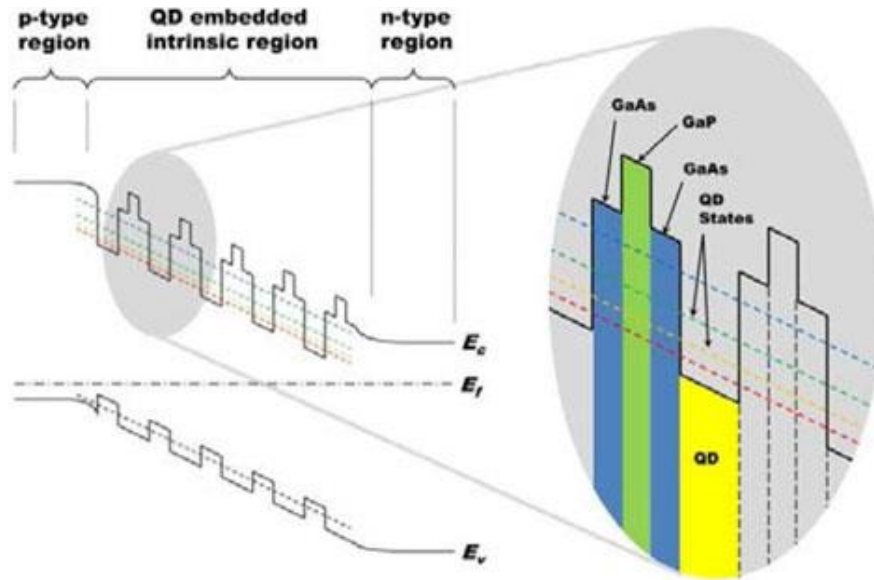


Fig 2.4 Energy band of QD GaAs p-i-n solar cell, illustrating conduction and valence band offset of superlattice layers in the intrinsic region of the device [8].

In 2013, Xiaoguang Yang et al [14] have studied the effect of doping the InAs/GaAs QDs solar cell by silicon (Si) in InAs QDs during the QD growth, the resulting J-V characteristic is shown in **Fig 2.5** and the extracted outputs in **Table 1**.

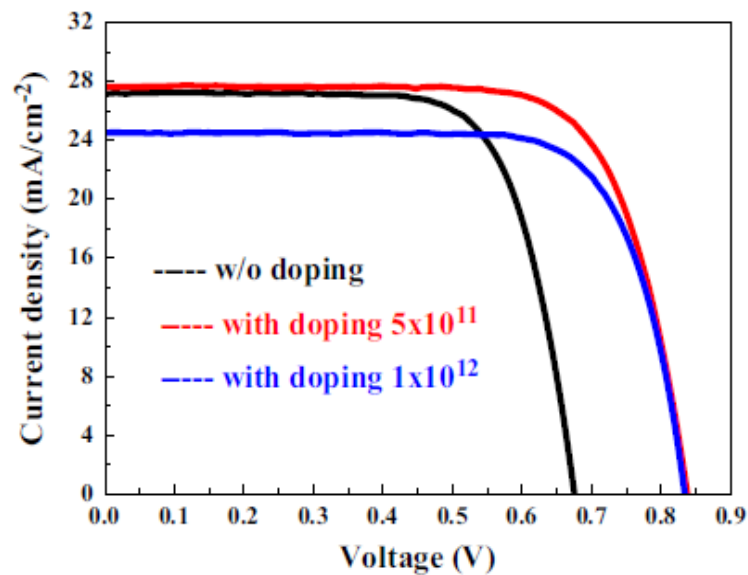


Fig 2.5 Current-voltage characteristics (J-V) of QD solar cell in [14].

Table 1 Outputs of Si-doped InAs/GaAs QD solar cell

Si-doping level (cm^{-2})	V_{oc} (mV)	J_{sc} (mA/cm ²)	FF (%)	η (%)
0	670	27.16	61.44	11.26
5×10^{11}	840	27.60	73.49	17.00
1×10^{12}	830	24.53	74.89	15.30

The authors interpreted the increase of efficiency of QD solar cell with doping due to the two possible reasons:

- The first one is that, Si–As has a shorter bond length than In–As, the substitution of Si for in will reduce the lattice mismatch between the InAs QDs and the GaAs capping layer, and these induce reduction in defect density.
- The second one, the defect states such as electron traps can be inactivated by the Si-doping, which could suppress the non-radiative process [14].

In 2016, Research group of center of Nanoscience and nanotechnologies from France used chemical beam epitaxy technique (CBE) for growth InAs/GaAs Quantum dots solar cell. Their results were not good enough but it is a promising growth technology for photovoltaic applications as it allows mass production with the lowest cost [9]. The resulting outputs are summarized in **Table 2**.

Table 2: Outputs parameters for the three solar cell reported in [9]

Device	V_{oc} (mV)	J_{sc} (mA/cm ²)	FF(%)	η (%)
Reference SC	861.4	18.8	64.2	10.4
2.5-nm QDSC	823.3	19.7	60.0	9.7
5-nm QDSC	792.3	19	60.2	9.1

Chapter 2 Numerical Modeling of Quantum dots solar cell by Silvaco-Atlas

This is one of the aims of this dissertation, we will try to simulate these solar cells and predict the main causes that give this range (9.1-10.4%) of the cell efficiency.

In the last years, Quantum dots has been used because of the Multi exciton generation or intermediate band (absorber layer) and also as a transport layer for electrons or holes. For example, it is possible to use the graphene, which has zero bandgap as QDs when we reduce the size of this material since it increases his bandgap up to 3.6 eV in addition to its good optical and electrical properties.

For example, in 2016 Senlin Diao et al fabricated solar cell with efficiency achieved 12.35% based on n-Silicon as a substrate and Graphene QDs as holes transport layer as show in **Fig. 2.6**.

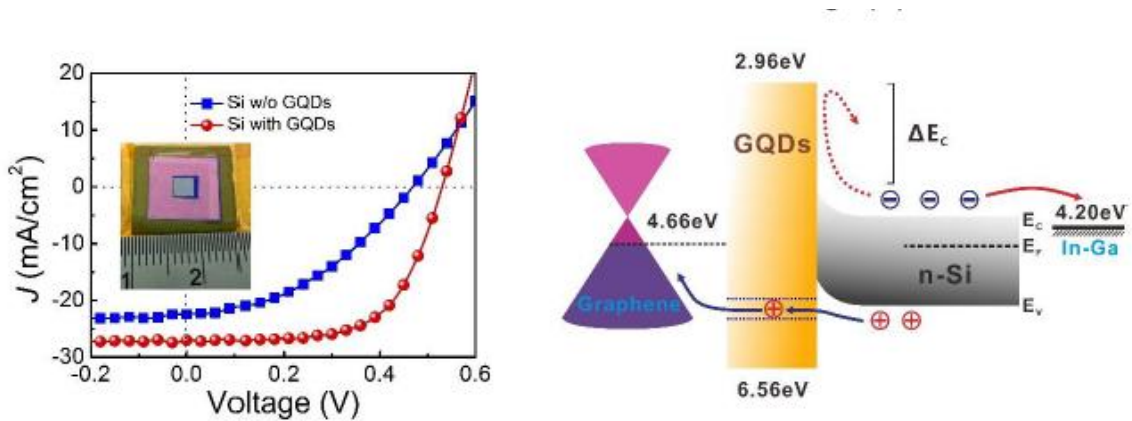


Figure 2.6: Structure and J-V characteristic of Graphene QD solar cell [10].

2.3 Physical mechanism of QDs solar cell

Advanced concepts for high efficiency solar cells such as Multi-Exciton Generation (MEG), and Intermediate-Band (IB) absorption in low-dimensional nanostructures are under focused research topics in recent years. Among various potential approaches, this paragraph is devoted to the device physics exactly the physical mechanism of quantum dot-based intermediate band (IB) solar cells and multiple exciton generation.

2.3.1 QDSC with intermediate band:

In this type of solar cell, it is required that QD be homogeneous and regularly and tightly placed in all three dimensions. This configuration then leads to formation of an Intermediate-Band (IB) or a superlattice miniband.

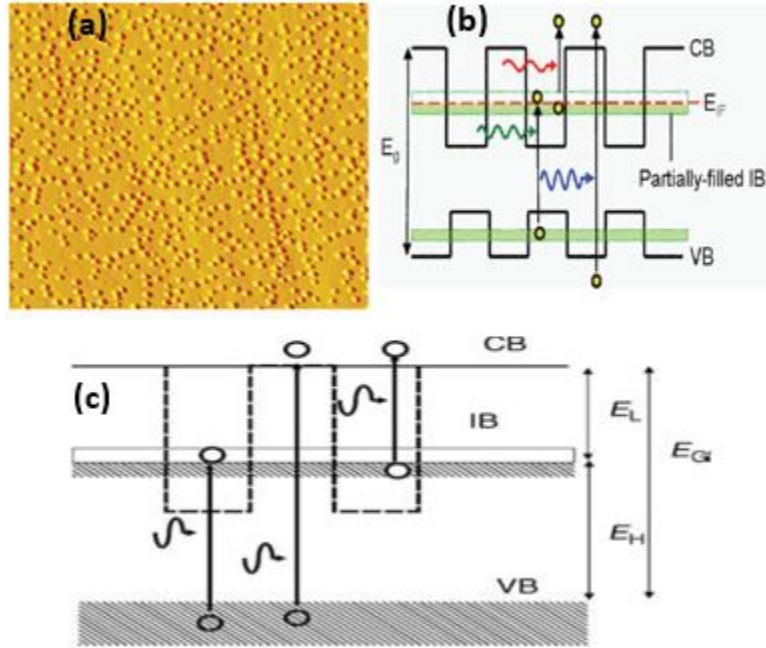


Fig 2.7- (a) -AFM image of self-assembled QDs grown by S-K growth mode of InAs QDs grown on GaAs [11]. (b)-Schematic energy band diagram of QD-IB solar cell with possible photo-absorption processes. The energy bandgap of host material and quasi-Fermi level of IB are given by E_g and E_{IF} , respectively [11]. (c) - Electron transition through intermediate band [2].

Secondly, IB states should ideally be half-filled with electrons in order to ensure an efficient pumping of electrons by providing both the empty states to receive electrons being photo-excited from the Valence Band (VB), and filled states to promote electrons to the Conduction Band (CB) via absorption of second sub-bandgap photons [11].

This type of QD offer the possibility for reducing thermal dissipation loss through absorption photons with energy lower than bandgap of matrix material (the host material

of the QD), the AFM (Atomic Force Microscopy) image of self-assembled QDs growth by S-K growth mode for InAs/GaAs QD and equivalent Band structure of IB solar cell as shown in **Fig. 2.7. (a)** and **Fig. 2.7. (b)**. Due to this intermediate band, electrons can jump from valence band to intermediate band temporarily, and then jump from intermediate band to conduction band with the help of another photon [2] as shown in **Fig. 2.7. (c)**

2.3.2 QDSCs with multiple exciton generation

One of the largest losses in a bulk or thin film solar cell occurs after the photon is absorbed, as photons with energy larger than the semiconductor bandgap produce charge carriers with excess kinetic energy, which is then dissipated via phonon emission.

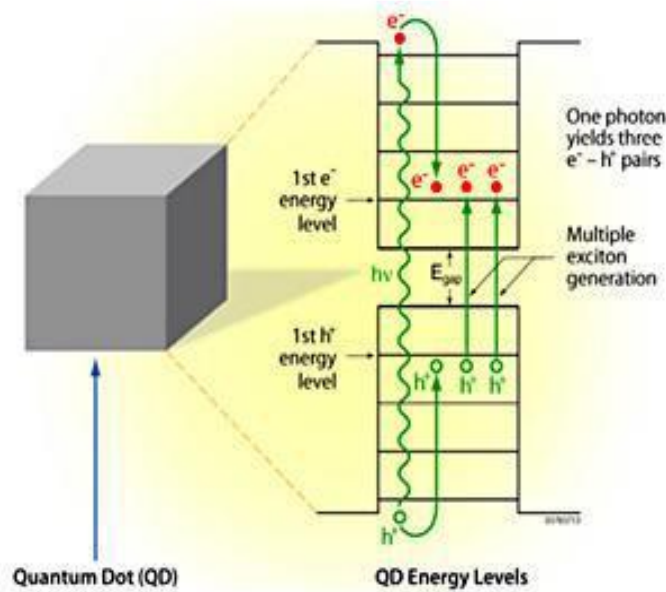


Fig 2.8 multiple exciton generation [3].

The most widely employed approach to reduce losses is through multi-junction PV devices. Multi-junction cells have produced PV efficiencies far beyond the Shockley Queisser limit [5] for single junction solar cells (to date 42% under un-concentrated AM 1.5 G conditions), but their high fabrication cost still renders large-scale deployment challenging another concept to minimize these losses is use QD solar cell When a single photon with sufficient energy is absorbed by solar cells, more than one electron-hole pair might be generated, this effect due to quantization energy of QD as shown in **Fig. 2.8**

2.4 Structure of QDSC

In this section, we will discuss the structure of Quantum dots fabricated by chemical beam epitaxy (CBE) by Research group of center of Nanoscience and nanotechnologies in university of paris-Saclay [9].

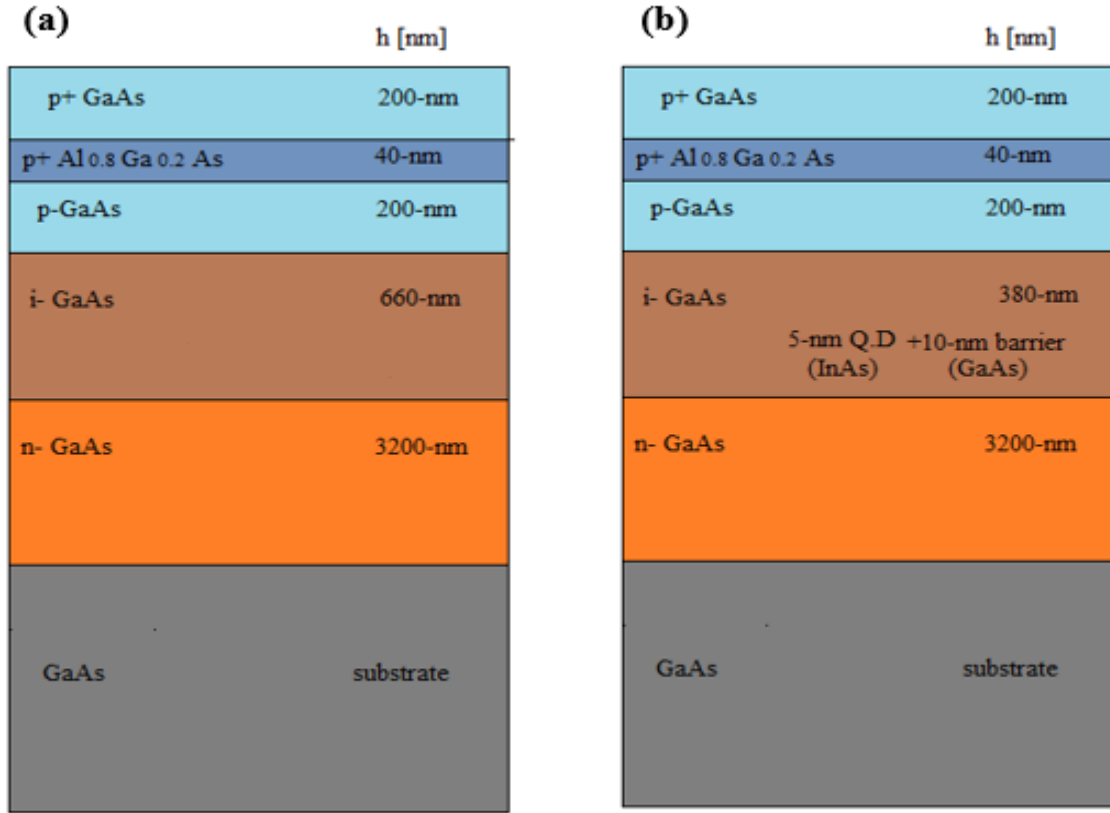


Fig 2.9-Structure of solar cell (a)-reference solar cell (b)-Q.D solar cell

Quantum dots are inserted in the intrinsic region of GaAs p-i-n solar cell and the material used, as quantum dot are InAs (Indium Arsenide). GaAs p-i-n solar cell were grown on n-type (001) GaAs substrate. For quantum dot solar cell, the intrinsic region that consist of a 30-nm thick GaAs buffer grown at 565°C followed by an undoped InAs QDs multilayer structure. Each QDs layer is separated by 30-nm thick GaAs.

For the reference cell (without QD), the intrinsic region of the solar cell consists of a 660-nm thick GaAs layer and 3200-nm thick GaAs as n-doped layer and a 200-nm p-doped GaAs.

Chapter 2 Numerical Modeling of Quantum dots solar cell by Silvaco-Atlas

The completed device structure is with 40-nm thick p+ doped $\text{Al}_{0.8}\text{Ga}_{0.2}\text{As}$ layer (that acts as a window layer) and a 200-nm thick p+ doped GaAs layer.

The used Quantum dots are with a height 5-nm and 2.5-nm. More detailed about the growth procedure of InAs QD are available in [9].

The alloy Ni/Ge/Au is used as a base contact (back contact) and the emitter grid (front contact) contains three layer Pt/Ti/Au respectively, the structure is shown in **Fig. 2.9** while **Fig. 2.10** shows AFM image of the distributions of QDs in the surface of GaAs [9].

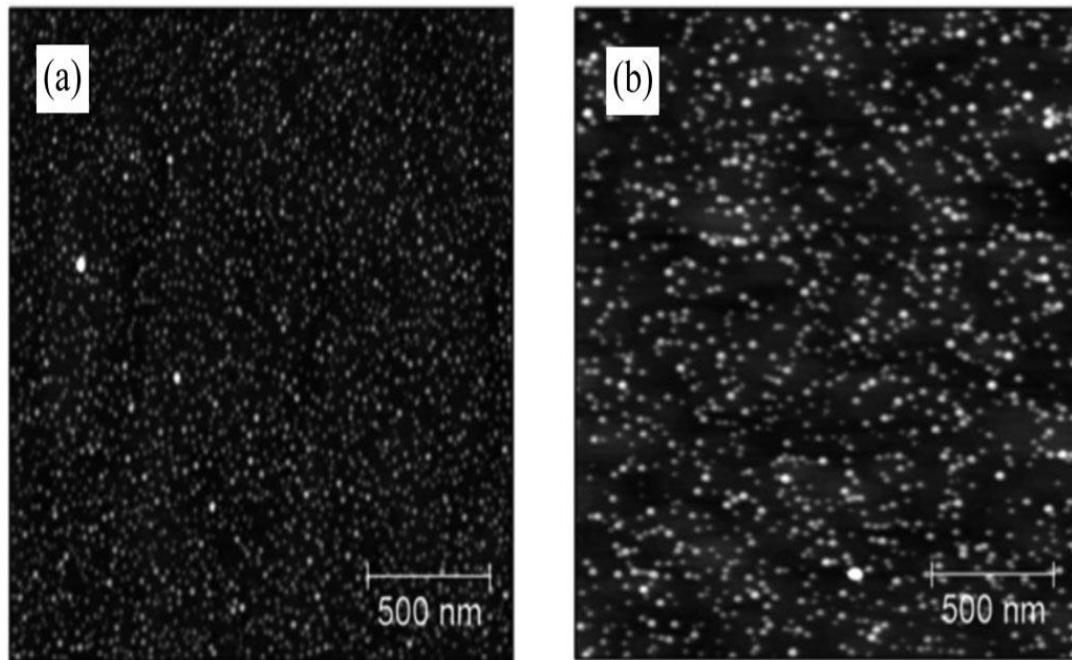


Fig 2.10 AFM image of QD in GaAs surface in two samples (a)-One and (b)-ten QD [9].

2.5 Simulation setup in Silvaco Atlas

2.5.1 Introduction

In this chapter, Silvaco TCAD Simulator is chosen as to simulate QDSC since it is specially designed for 2D and 3D simulations.

Silvaco TCAD (Technology Computer Aided Design) is a powerful device design and simulation simulator, including both semiconductor process simulation and device simulation. This simulator is developed by Silvaco [12].

Chapter 2 Numerical Modeling of Quantum dots solar cell by Silvaco-Atlas

As shown in **Fig. 2.11**, Silvaco TCAD contains many different parts, such as interactive tools DeckBuild and Tonyplot, process simulator Athena, device simulator Atlas, structure and mesh editor DevEdit, and so on. **Fig. 2.11** describes the flow diagram when simulating through Silvaco TCAD. All these parts are organized together through DeckBuild interface.

From **Fig. 2.11**, we can see that device simulator Atlas is the core part of Silvaco TCAD simulator. It can simulate many characteristics of a semiconductor device completely, including electrical behavior, optical behavior, thermal behavior, and so on. Atlas provides an easy-to-use, which is based on physics. In addition, Atlas affords a large number of physical calculation models for users to choose [3].

As a device simulator, Atlas owns a full set of functions from building models to calculating out results. All these functions are achieved through statement description. Atlas statements can be classified into different groups by five different functions, which are structure specification, material models specification, numerical method selection, solution specification, results analysis, respectively. **Fig. 2.12** shows primary statements in each Atlas command groups.

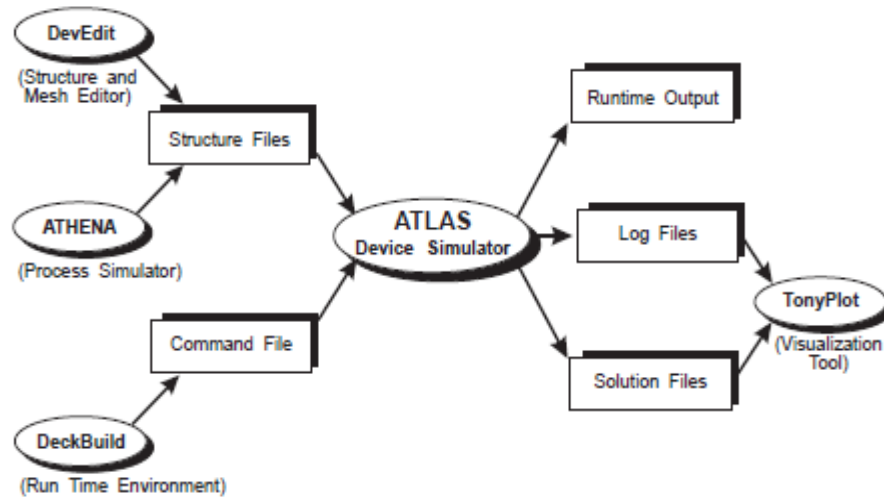


Fig 2.11 Simulation flow diagram of Silvaco TCAD [12].

<i>Group</i>	<i>Statements</i>
1. Structure Specification	MESH REGION ELECTRODE DOPING
2. Material Models Specification	MATERIAL MODELS CONTACT INTERFACE
3. Numerical Method Selection	METHOD
4. Solution Specification	LOG SOLVE LOAD SAVE
5. Results Analysis	EXTRACT TONYLOT

Fig2.12 Flow chart and command groups of Atlas [12].

Structure specification: Including the division of meshes, definition of regions with different materials and type of material and doping concentration, definition of electrodes. First, the division of grids can be controlled by command “MESH”, as example shown below:

```
x.m loc=0.0 s=0.1
x.m loc=1.0 s=0.1
y.m loc=0 s=0.1
y.m loc=3.0 s=0.1
```

“x.m” is used to define grids in landscape orientation, and “y.m” is used to define grids in portrait orientation. “loc” is the location where the grids will exit and “s” means the density or spacing between two successive nodes.

Second, the definition of regions can be controlled by command “REGION”, as examples shown below:

```
region material=GaAs thick=0.2 accept=1e19 ny=10 nx=10 material=GaAs
```

Chapter 2 Numerical Modeling of Quantum dots solar cell by Silvaco-Atlas

“thick” used to define the thickness of this region and “accept” used to define for p-type semiconductor or “donor” for n-type and “nx”, “ny” used to define the number of nodes and “material” is used to define the material used in this region.

Thirdly, electrodes and material used can be defined by using commands below:

```
electrode name=anode material=Gold x.min=0.45 x.max=0.55 y.min=0 y.max=0.2  
electrode name=cathode bottom
```

Material models specification: Including setup of material parameters (band gap, absorption coefficient, minority lifetime, electron affinity etc.), choose of physical models, specification of contact characteristics, and definition of interface properties.

First, the parameters and characteristics of materials used in simulation models can be defined by command “MATERIAL”, as the example shown below:

```
material mat=InAs EG300=0.65 permittivity=14.6 affinity=4.9 Nc300=8.7e16\  
Nv300=6.6e18 index.file=InAs1.nk out.index=InAs \  
user.group=semiconductor user.default=InAs MUN=22600 MUP=200
```

Among them, “EG300” means energy gap at 300K (unit: eV). “permittivity” means dielectric constant. “affinity” means electron affinity (unit: eV). “Nc300” and “Nv300” mean effective density of states in the conduction band and valence band, respectively (unit: cm^{-3}).

“index.file” means the refraction index. “user.group” Specifies the material group for the user-defined material. USER.GROUP can be either semiconductor, insulator, or conductor. “user.default” specifies which material the user-defined material should use for its default parameters and “MUN” and “MUP” means mobility of electrons and holes respectively.

Second, we need to choose physical calculation models by using command “MODELS”, as the example shown below:

```
model fermi SRH conmob optr print
```

“fermi” refers to the model that Fermi-Dirac statistics is used and SRH (Shockley Read Hall) means the Shockley Read Hall recombination model is used and “conmob” refers to

Chapter 2 Numerical Modeling of Quantum dots solar cell by Silvaco-Atlas

the model that mobility depends on concentration of impurity. "print" does not refer to any model, but means all models and material parameters will output in tabular form, and other models.

Thirdly, we can define the surface recombination rate by using command "INTERFACE", as the example shown below:

```
interface x.min=0.45 x.max=0.55 y.min=-0.05 y.max=0.05 s.n=1e2 s.p=1e2
interface x.min=0 x.max=1 y.min=13.8-0.05 y.max=13.8 s.n=1e2 s.p=1e2
```

"s.p" and "s.n" means the surface recombination rate of holes and electrons .

Numerical method selection: Computer simulation is based on numerical calculation. To make sure that the calculation can converge, numerical method should be selected properly. In Atlas, there are Newton iteration method, Gummel iteration method, Block iteration method, and combination iteration method [3].

For example:

```
method newton
```

Solution specification:

After finishing building the structure and choosing proper physical models and numerical methods, next step is to apply illumination and bias voltage, and then we can finally obtain all the characteristics we need from a solar cell. Here, example will be presented in order to clearly describe this part of statements in Atlas. However, this example, we will obtain one of the most important characteristic of solar cell: I-V (J-V) curve.

I-V (J-V) characteristic is one of the most important properties for a solar cell. From the I-V (J-V) curve, we can also obtain the short circuit current and open circuit voltage.

The solar cell was exposed to a 1-sun illumination AM1.5 with normal-incident light source and intensity of 100 (mW/cm²). This can be simulated using Silvaco using BEAM command with input file power "solarex03_15.spec" as follows:

```
beam num=1 x.orig=0.5 y.orig=-0.5 angle=90 power.file=solarex03_15.spec\
out.power=solarex03_15.log wavel.start=0.305 wavel.end=1.8 wavel.num=300 normalize
```

Chapter 2 Numerical Modeling of Quantum dots solar cell by Silvaco-Atlas

where “x.orig” and “y.orig” define the source position and “wavel.start”, “wavel.end” and “wavel.num” define the domain of wavelength , **Fig 2.13** below shows the used solar spectrum.

After define the illumination, next step is apply bias voltage and change their values, as shown below:

```
solve b1=1e-08
solve b1=1e-07
solve b1=1e-05
solve b1=1e-04
solve b1=1e-03
solve b1=1e-02
solve b1=0.1
solve b1=0.2
solve b1=1
solve vanode=0 vstep=0.05 vfinal=0.3 name=anode
solve vanode=0.32 vstep=0.02 vfinal=1.2 name=anode
```

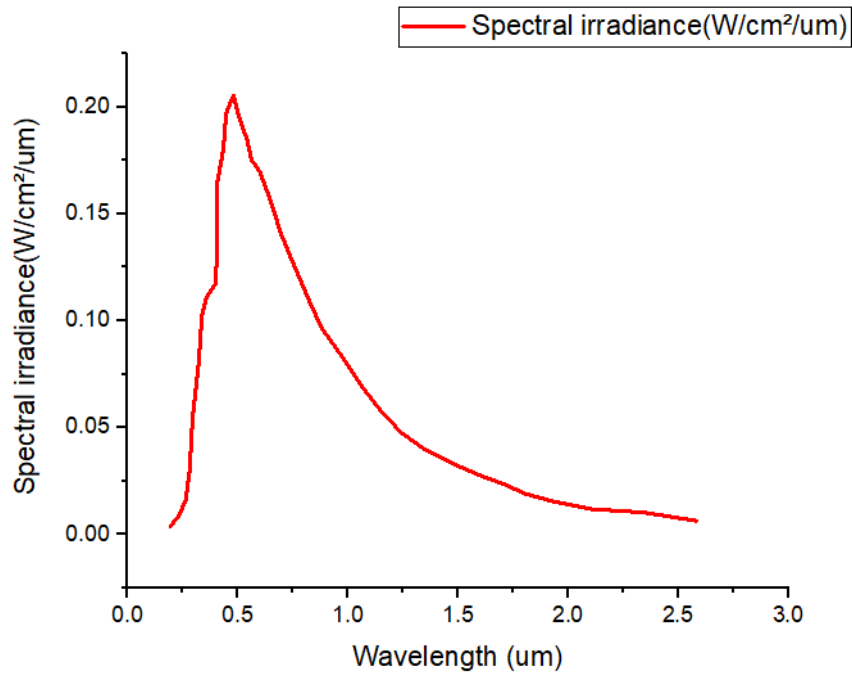


Fig 2.13 solar spectrum used in this simulation

Results analysis:

After finishing the calculation and stored the results in records files, we need to plot and extract the results, for this step we use the commands “tonyplot” and “extract”.

The first thing we need to do is to tell Atlas what characteristics we want to obtain.

For this step, we use the command “output” as the example shown below:

```
output opt.int band.temp band.param val.band con.band
```

“opt.int” means the optical intensity and “band.temp” means the variation of bandgap energy with temperature and “band. Param” means all band parameters (such as E_g , n_i , N_c , N_v)

“val.band” and “con.band” means valance band and conduction band respectively. Next step is to use the graphical characteristic viewer, which is built inside the visualization tool TonyPlot, as shown in **Fig.2.14**.

We can choose any parameter we have required in command “OUTPUT” in the Quantity icon in **Fig.2.14**.

The other command “extract” is used to extract useful values from simulation results, which are stored in log files.

For example, we use this command for extract J_{sc} and V_{oc} from the J-V characteristic as shown in example below:

```
extract name="IV" curve(v."anode",i."cathode"*1e03*1e8) outfile="IVcurvlight.dat"
extract name="Jsc" y.val from curve(v."anode", i."anode") where x.val=0.0
extract name="JscmAcm2" $Jsc*1e03*1e8*-1
extract name="Voc" x.val from curve(v."anode", i."anode") where y.val=0.0
```

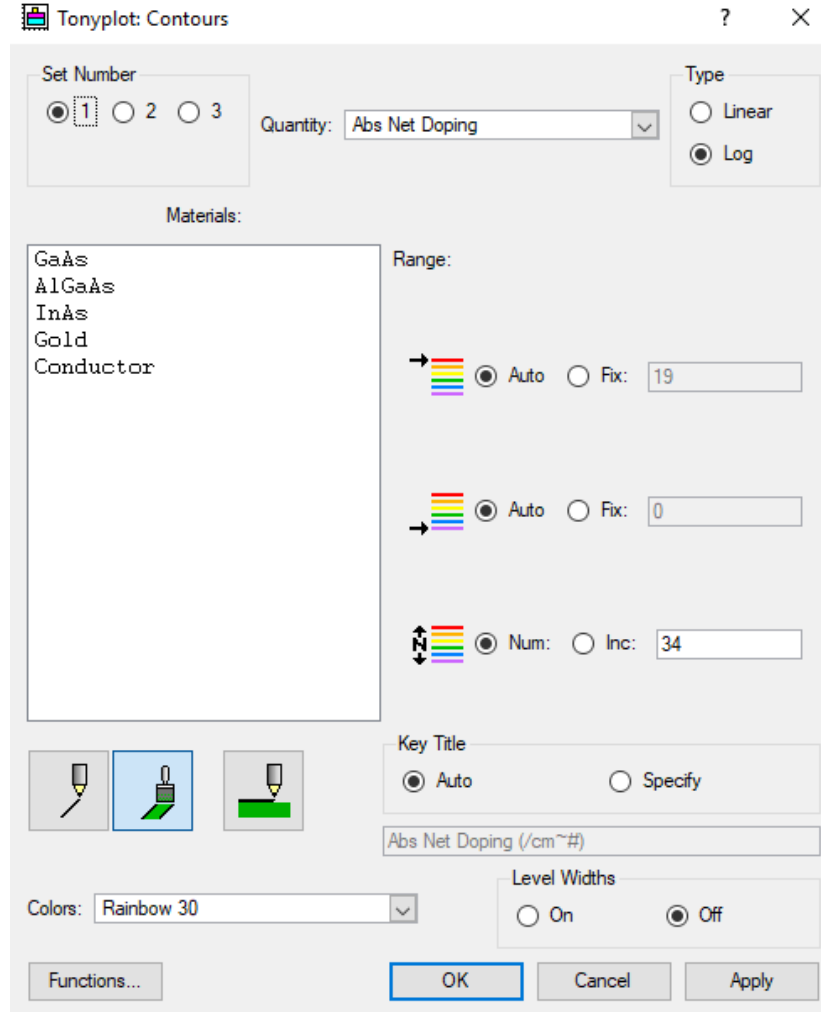


Fig 2.14 Graphical characteristic viewer

2.5.2 Simulation steps for standard solar cell

In the first step, we use Atlas to simulate a conventional p-i-n GaAs solar cell with the same structure as in **Fig.2.8. (a)** [9].

The solar cell includes (**Fig.2.15**) $10\mu\text{m}$ n^+ -GaAs substrate, the other layers are p^+ -GaAs, $p\text{-Al}_{0.8}\text{Ga}_{0.2}\text{As}$, $p\text{-GaAs}$, $i\text{-GaAs}$, $n\text{-GaAs}$ with thicknesses of 200-nm, 40-nm, 200-nm, 660-nm and 3200-nm, respectively. The respective doping of these layers is: $1 \times 10^{19}\text{cm}^{-3}$, $1 \times 10^{18}\text{cm}^{-3}$, $1 \times 10^{18}\text{cm}^{-3}$, $1 \times 10^{19}\text{cm}^{-3}$ and $1 \times 10^{19}\text{cm}^{-3}$. Gold is used as front contact.

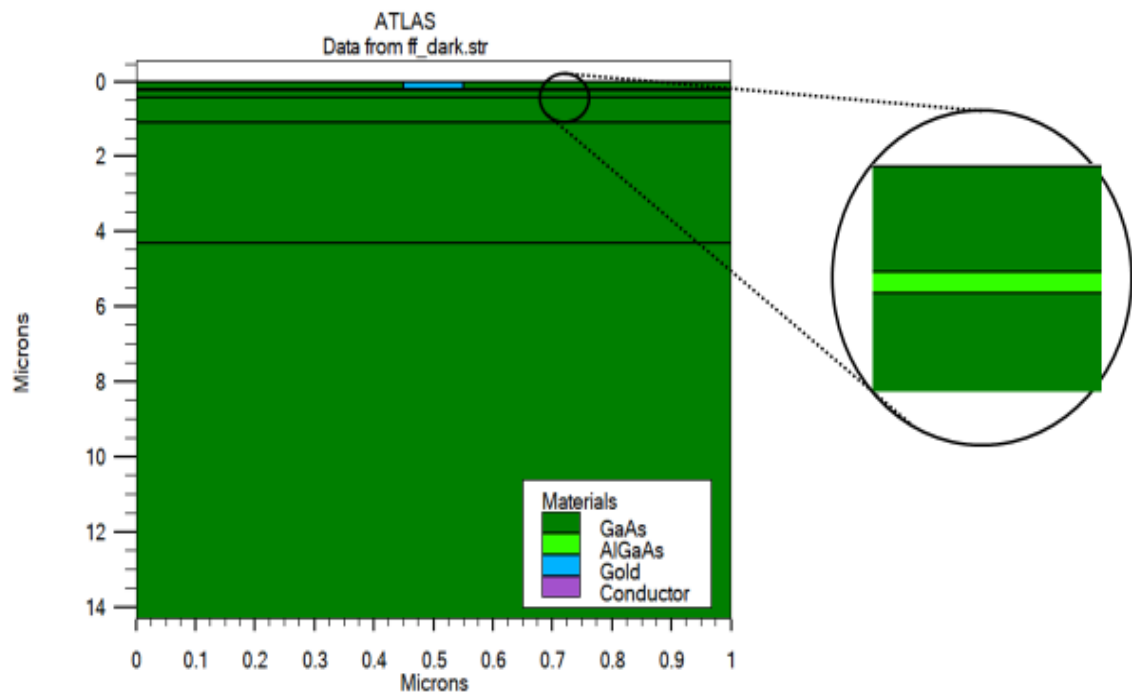


Fig.2.15 structure of standard p-i-n GaAs solar cell

The J-V characteristics of standard solar cell obtained by Silvaco is shown in **Fig 2.16**

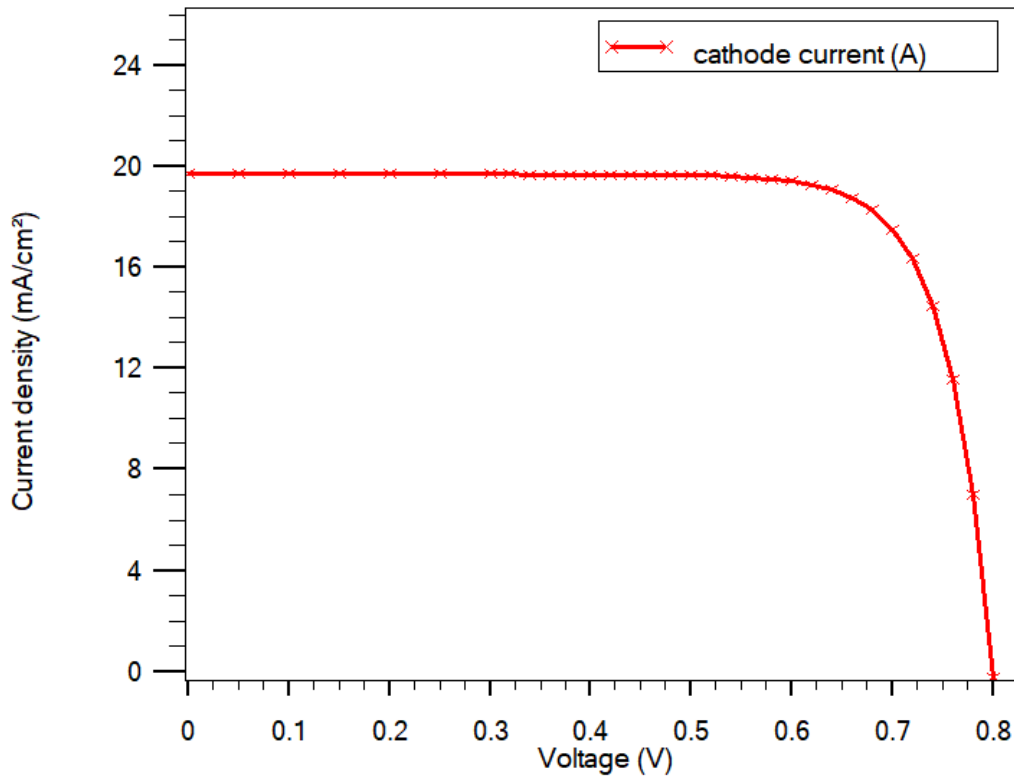


Fig 2.16 J-V characteristics of standard solar cell

2.5.3 Simulation of QDSC

In this dissertation for the QD solar cell, the simulation by Atlas is performed for 2D InAs/GaAs QD solar cell. The solar cell is designed as the standard p-i-n GaAs structure where ten layers of QD is embedded in the intrinsic region of the cell. The only difference is the thickness of intrinsic region because in the p-i-n GaAs structure used here the thickness of intrinsic region depends in the number of QD layers.

For simplicity in our 2D calculation, each QD is modeled by a rectangle [13] with diameter and height of 90-nm and 5-nm, respectively, distance between the layers is 30-nm, the distance between the QD in the same layer is 10-nm, and the thickness of intrinsic region is 380-nm as shown in **Fig 2.17** and the band diagram shown **Fig 2.18**.

In ATLAS conventional solar cell is described by the Poisson, continuity equation and drift-diffusion transport equations, and such differential equations are solved by the finite element method (F.E.M) [12].

Chapter 2 Numerical Modeling of Quantum dots solar cell by Silvaco-Atlas

After solving these equations, we can find electrostatic potential (ϕ) and the electron and hole concentrations(n, p).

However, in QDSC the idea is quite different, in addition to classical solution in bulk regions, we insert the quantum solution in the QD region.

For bulk regions, the electrons and holes concentrations are described in terms of the effective density of states (N_c and N_v), conduction and valance band edge energies (E_c and E_v), and quasi-Fermi levels (E_{Fn} and E_{Fp}):

$$n_{bulk} = N_c F_{1/2} \left(\frac{E_{Fn} - E_c}{K_B T} \right) \quad (2.1)$$

$$p_{bulk} = N_v F_{1/2} \left(\frac{E_v - E_{Fp}}{K_B T} \right) \quad (2.2)$$

Where K_B is Boltzmann constant, T is the temperature, and $F_{1/2}$ is Fermi-Dirac integral of order 1/2.

For the 2D modeled QDs the K.P (Kroning-Penney) model (for Zincblend structure) is used for self-consistent solution of Schrödinger-Poisson model and the carrier concentrations, depending on the carrier wave function (Ψ_i and Ψ_j) and eigen energies (E_i and E_j), are given by [13]:

$$n_{QD} = 2 \frac{\sqrt{2 m_e^* K_B T}}{h} \sum_i |\Psi_i|^2 F_{-1/2} \left(-\frac{E_i - E_F}{K_B T} \right) \quad (2.3)$$

$$p_{QD} = 2 \frac{\sqrt{2 m_h^* K_B T}}{h} \sum_j |\Psi_j|^2 F_{-1/2} \left(-\frac{E_f - E_j}{K_B T} \right) \quad (2.4)$$

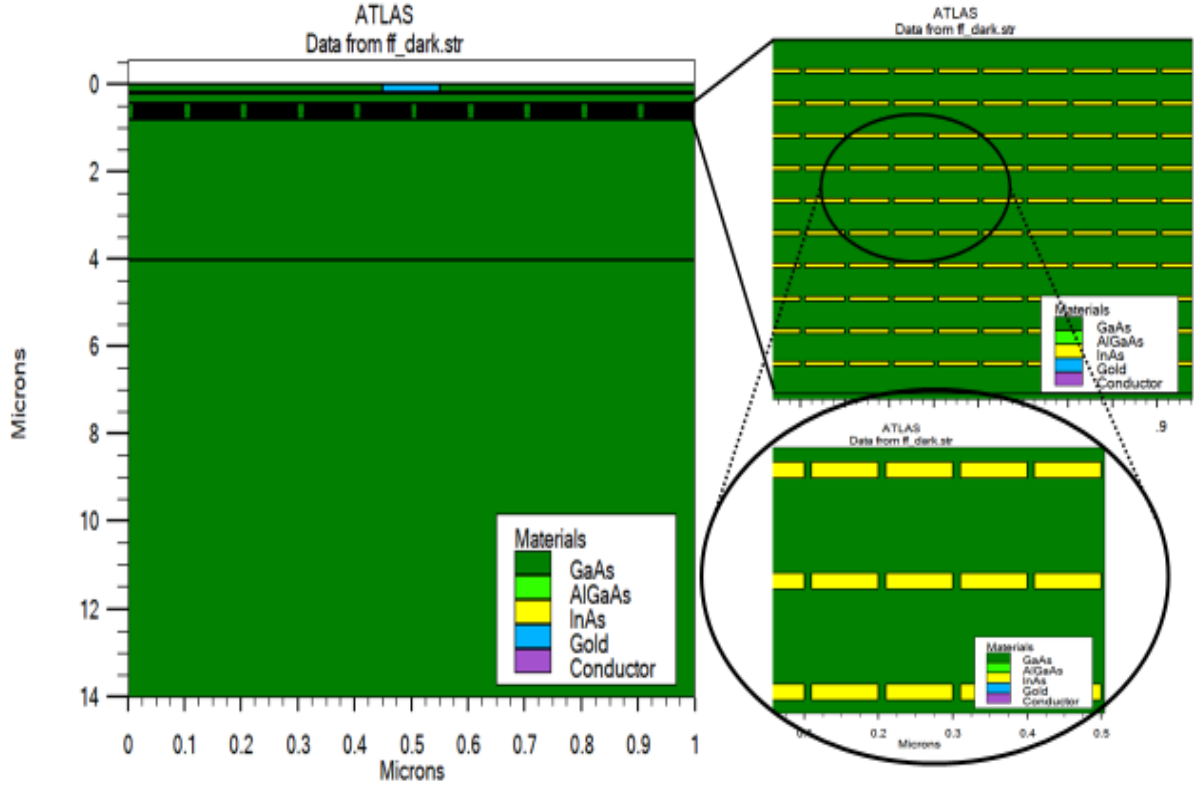


Fig.2.17 2D schematic of InAs/GaAs QD solar cell structure

Where m_e^* and m_h^* are the electron and hole effective masses, E_f is the Fermi level, and $F_{-1/2}$ is The Fermi-Dirac integral of order $-1/2$. The carrier wave function and eigen energies are obtained by numerically solving the 2D Schrödinger equation [13]:

$$\frac{\hbar^2}{2} \left[\frac{\partial}{\partial x} \left(\frac{1}{m_e^*} \frac{\partial \psi_i}{\partial x} \right) + \frac{\partial}{\partial y} \left(\frac{1}{m_e^*} \frac{\partial \psi_i}{\partial y} \right) \right] + E_c \psi_i = E_i \psi_i \quad (2.5)$$

$$\frac{\hbar^2}{2} \left[\frac{\partial}{\partial x} \left(\frac{1}{m_h^*} \frac{\partial \psi_j}{\partial x} \right) + \frac{\partial}{\partial y} \left(\frac{1}{m_h^*} \frac{\partial \psi_j}{\partial y} \right) \right] - E_v \psi_j = E_j \psi_j \quad (2.6)$$

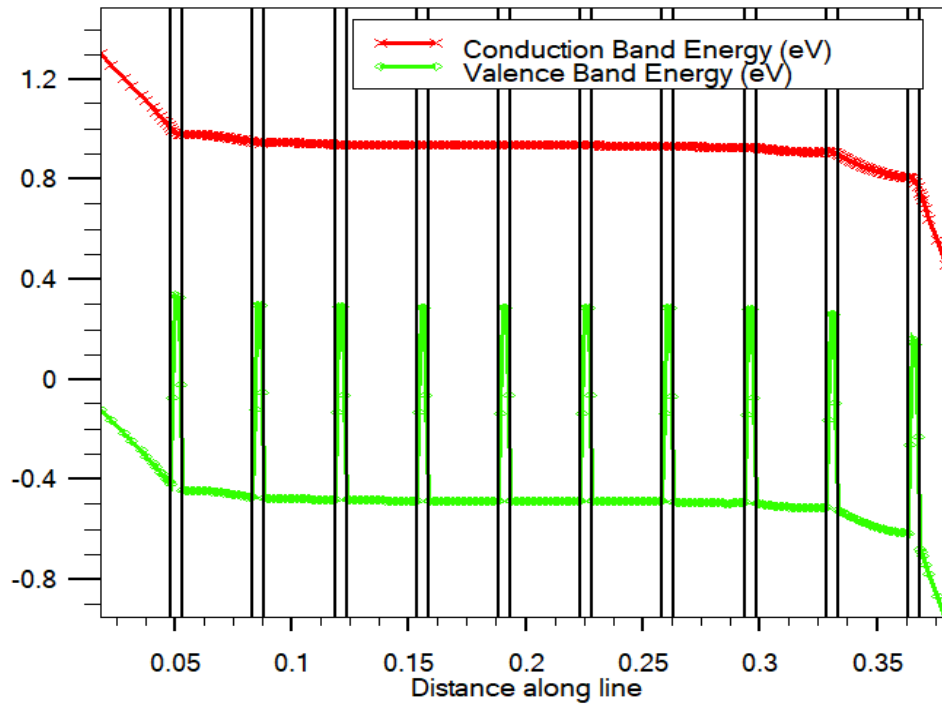


Figure 2.18 Band diagram of QDSC

In which \hbar is the reduced Planck constant. Each energy eigenvalue $E_i(E_j)$ corresponds to its eigenfunction or wave function $\Psi_i(\Psi_j)$. It should be noted that the carrier wave function and the conduction and valance band energies are position-dependent in the xy-plane.

In the self-consistent model after calculating the conventional and Quantum concentration of electrons and holes ($n_{bulk}, p_{bulk}, n_{QD}, p_{QD}$) in the QD and bulk region, we find [13]:

$$n = n_{bulk} + n_{QD} \quad (2.7)$$

$$p = p_{bulk} + p_{QD} \quad (2.8)$$

In this type of solar cell, the carrier concentrations calculated from the Schrödinger equations (n_{QD}, p_{QD}) and bulk region (n_{bulk}, p_{bulk}) determines the potential V in the Poisson equation, while E_c and E_v which entail the carrier concentrations in the QDs region are simultaneously affected by the potential V . Therefore, the variable V , n_{QD} and p_{QD} must

Chapter 2 Numerical Modeling of Quantum dots solar cell by Silvaco-Atlas

be solved consistently. Thus, the current densities due to thermionic emission and tunneling are necessary to be considered [13].

Fig.2.19 shows an example of wavefunctions of electrons and holes of the studied QDSC and **Fig.2.20** show an example of the calculated J-V characteristics of ten InAs/GaAs QD layers solar cell.

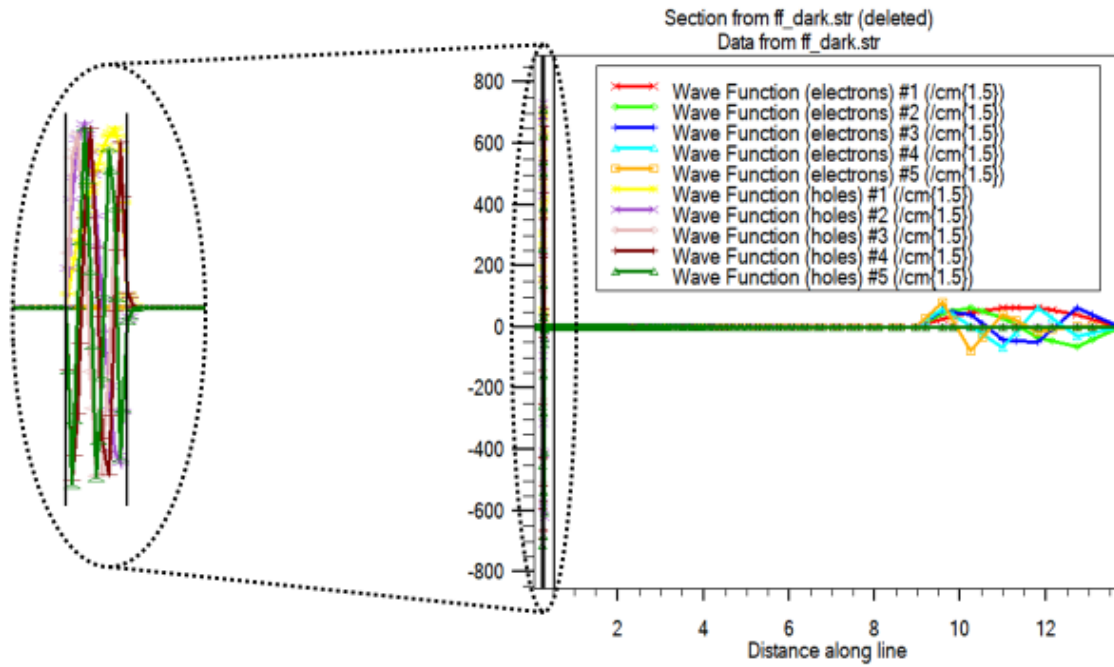


Fig.2.19 Wavefunction of electrons and holes simulated along the structure by Silvaco Atlas.

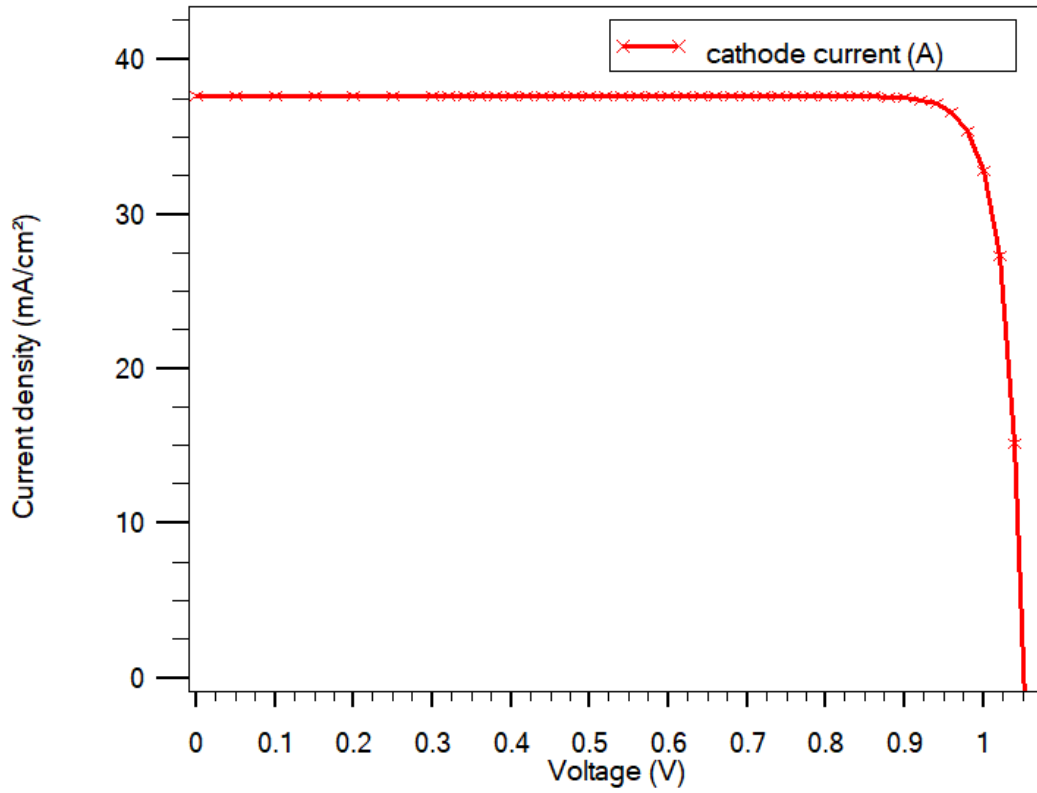


Fig 2.20 J-V characteristics of QDSC calculated by SILVACO-Atlas

Chapter 2 Numerical Modeling of Quantum dots solar cell by Silvaco-Atlas

References:

- [1] A. Marti, N. Lopez, E. Antolin, E. Canovas, A. Luque, C. Stanley, C. Farmer, P. Diaz, Emitter degradation in quantum dot intermediate band solar cells, *Applied Physics Letters* 90 (2007) 233510.
- [2] A. Luque, A. Marti, A. J. Nozik, Solar cells based on quantum dots: multiple exciton generation and intermediate bands, *MRS bulletin* 32 (2007) 236-241.
- [3] Boqun Dong. Modeling and Simulation of InAs/GaAs Quantum Dot Solar Cells in SILVACO TCAD, Master of Science, 2014, USA, university of Washington
- [4] A. Belghachi, Theoretical calculation of the efficiency limit of solar cells, in: *solar cells- New Approaches and Reviews*, IntechOpen, 2015.
- [5] W. Shockley, H. J. Queisser, Detailed balance limit of efficiency of P-N junction solar cells, *Journal of applied physics* 32 (1961) 510-519.
- [6] K. Tanabe, D. Guimard, D. Bordel, Y. Arakawa, high-efficiency quantum dot solar cell by metalorganic chemical vapor deposition, *Applied Physics Letters* 100 (2012) 193905.
- [7] R. Laghnavarapu, M. El-Emawy, N. Nuntawong, A. Moscho, L. Lester, D. Huffaker, Improved device performance of InAs/GaAs quantum dot solar cells with GaP strain compensation layers," *Applied Physics Letters*, 91(2007), 243115.
- [8] C. G. Bailey, D. V. Forbes, S. J. Polly, Z. S. Bittner, Y. Dai, C. Mackos, R. P. Raffaele, S. M. Hubbard, Open-Circuit Voltage improvement of InAs/GaAs quantum dots solar cells using reduced InAs coverage, *IEEE, Journal of Photovoltaics* 2 (2012), 269-275.
- [9] J. Zribi, B. Ilahi, B. Paquette, A. Jaouad, O. Theriault, K. Hinzer, R. Cheriton, G. Patriarche, S. Fafard, V. Aimez, et al, Effect of dot-height truncation on the device performance of multilayer InAs/GaAs quantum dot solar cells, *IEEE Journal of Photovoltaics* 6 (2016) 584-589.
- [10] S. Diao, X. Zhang, Z. Shao, K. Ding, J. Jie, X. Zhang, 12.35% Efficient Graphene Quantum Dots/Silicon Heterojunction Solar Cells using Graphene Transparent Electrode, *Nano Energy* 31 (2017) 359-366.
- [11] L. Fara, *Advanced Solar Cell Materials, Technology, Modeling and Simulation*, IGI Global, 2012.

Chapter 2 Numerical Modeling of Quantum dots solar cell by Silvaco-Atlas

[12] Silvaco-TCAD. Atlas user's manual: device simulation software. California: Silvaco International. (2018).

[13] M. Kunruga, Two-dimensional simulation of GaAsSb/GaAs quantum dot solar cells, *Journal of Physics D: Applied Physics* 51 (2018) 225101.

[14] X. Yang, K. Wang, Y. Gu, H. Ni, X. Wang, Z. Wang, Improved efficiency of InAs/GaAs quantum dots solar cell by Si-doping, *Solar Energy Materials and Solar cells* 113 (2013) 144-147.

Chapter 3

Results and discussion

3.1 Introduction

In this chapter, we present the simulation results of the studied InAs/GaAs QDSC using SILVACO-ATLAS. This study is divided into three steps. In the first step, we'll simulate the ideal QDCS and effect of number of QD layers and doping on its properties. In the second step, the presence of defects is taking into account to reproduce the experimental J-V characteristic of InAs/GaAs QDSC. The effect of QD layers number and doping in this case is also checked and in contrast to the ideal case, the experimental observations are well reproduced. Finally, an optimization process is proposed based on the conception of the QDSC.

3.2 Ideal QDs solar cell

We begin this section by presenting the classical J-V characteristic of GaAs-p-i-n solar cell (to compare it next with the QDSC), **Fig 3.1**. The structure of this solar cell has been presented in chapter 2. The extracted electrical outputs are in **Table 1**.

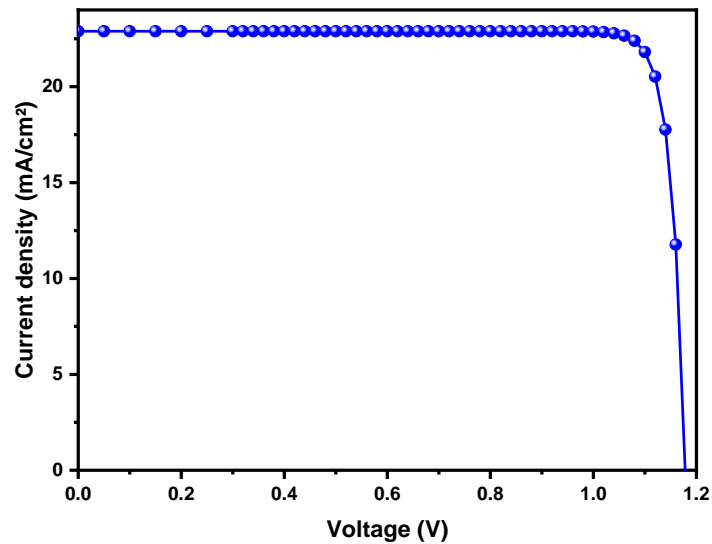
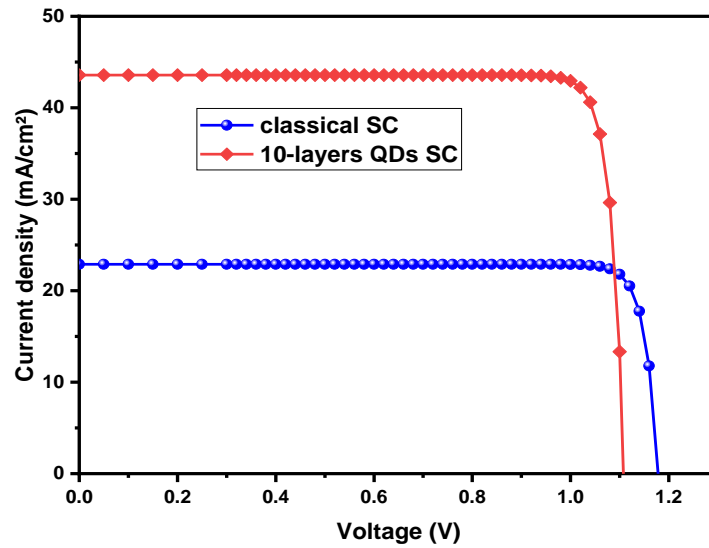


Fig 3.1 J-V characteristics of classical GaAs-p-i-n solar cell

Table 1 Outputs of classical solar cell

Device	$V_{oc}(mV)$	$J_{sc}(mA/cm^2)$	$FF\%$	$\eta\%$
p-i-n SC	1178.13	22.89	89.65	24.18

For the QDSC, the structure contains 10-QDs layers in the intrinsic region (Structure in chapter 2). The obtained J-V characteristic in the ideal case is presented in **Fig.3.2** and **Table 2** summarizes the extracted outputs.

**Fig 3.2** J-V characteristic of 10-layers QDs solar cell compared to classical case.**Table 2** Outputs of 10-layers QDSC

Device	$V_{oc}(mV)$	$J_{sc}(mA/cm^2)$	$FF\%$	$\eta\%$
QDs SC	1107.55	43.58	89.18	43.05

By ideal case for the QDSC we mean that there are no defects in the structure. Then the recombination is omitted. The increase in J_{sc} compared to conventional solar cell due to the decrease of the effective bandgap of the solar cell [1], otherwise, due to the absorption of photon less than the bandgap of GaAs material [2]. The decrease in V_{oc} results from the

reduction of the effective bandgap of the solar cell [1]. In addition, the QDSC present a conversion efficiency of 43.5 % which is considerably higher than 18.5% obtained for the ideal MQWSC (chapter 1).

3.2.1 Effect of number of quantum dots layers

The number of QDs layers is increased from 1 to 10. The obtained J-V characteristics are presented in **Fig.3.3** and the related outputs in **Table 3**. With the increase of the QDs layers number V_{oc} , J_{sc} and η increase while FF increases slightly until 5 QD layers then it decreases also slightly after.

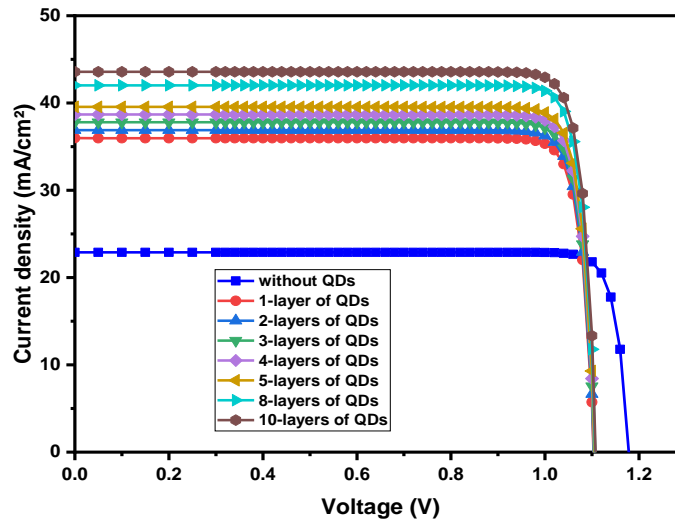


Fig 3.3 J-V characteristics for different number of QDs

Table 3 Effect of number of QD layers on outputs

Number of layers	$V_{oc}(mV)$	$J_{sc}(mA/cm^2)$	$FF\%$	$\eta\%$
1	1103.24	35.97	89.02	35.33
2	1103.77	36.90	89.02	36.25
3	1104.28	37.80	89.02	37.16
4	1104.78	38.68	89.03	38.05
5	1105.27	39.55	89.94	38.94
8	1106.67	42.02	89.14	41.46
10	1107.55	43.58	89.18	43.05

These results agree with most numerical works[3][4]. The significant improve mainly in current density is explained by the device absorption enhancement with the increase of the number of QDs layers[4]. However, experiment results are completely different [6-14].

3.2.2 Effect of doping QD layers

We are interested in the effect of doping because in several experimental papers doping is used as a means to improve the quality of QD cells. But it is not clear if the doping role is simply the increase of free carrier densities or contributes to the QDSC improvement by another process. To shed light on this point we should first simulate the doping effect in the ideal case.

The effect of doping increase from 1×10^{16} to $1 \times 10^{19} cm^{-3}$ in the 10-layers QDs solar cell is shown in **Table 4**.

Table 4 Effect of doping in the 10-layers QDs solar cell

Doping(cm^{-3})	$V_{oc}(mV)$	$J_{sc}(mA/cm^2)$	$FF\%$	$\eta\%$
0	1107.55	43.58	89.18	43.05
1×10^{16}	1107.55	43.58	89.18	43.05
1×10^{17}	1107.55	43.58	89.18	43.05
1×10^{18}	1107.55	43.58	89.18	43.05
1×10^{19}	1107.55	43.58	89.19	43.05

As obtained, the doping does not affect solar cell properties, in contrast to experimental results[5]. This probably, due to the absence of defects and recombination centers that make doping more active.

3.3 Real InAs/GaAs QDs solar cell

In this section, we try to reproduce the real J-V characteristic of the QDSC by taking into account the presence of defects in the structure. Simulation allows us to precisely determine the main type of defects that gives J-V shape closer to experimental measurement.

Fig 3.4 shows a comparison between experimental and ideal 10-layers QDSC characteristics where the disagreement is huge.

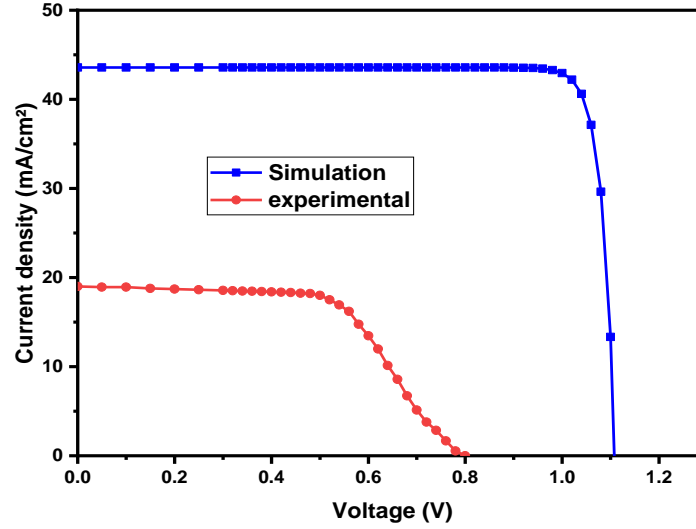
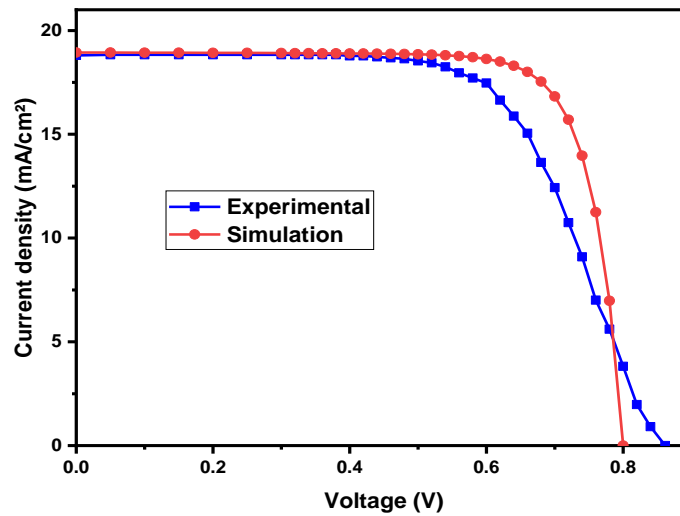


Fig 3.4 Comparison between experimental and ideal J-VQDSC curves.

Defects that can subsist in the structure are classified onto classic defects and further others related to QDs. To clarify the nature of the original defects in the classical structure, we have to introduce the intrinsic defects often reported by DLTS characterization works in GaAs [8]. Three types are reported: two electron traps and one hole trap. The energy level of one of the electron trap is located very close to the hole trap, in the mid gap. Then these two traps can be considered as one recombination level. The parameters of the intrinsic defect levels are summarized in **Table 5** [8]. The comparison between the classical GaAs-p-i-n J-V curve (taking into account intrinsic defects) and the experimental one is shown in **Fig.3.5**. The extracted outputs are in **Table 6**.

Table 5 Properties of defect levels for classical GaAs-p-i-n SC [8].

Defect Level	Type	$E_c - E_T$ (meV)	Density(cm^{-3})	Capture cross section (cm^2)	
				σ_n	σ_p
E4-H3	Recombination center	700	1×10^{14}	1×10^{-14}	1×10^{-14}
E5	Electron trap	960	1×10^{13}	2×10^{-12}	1×10^{-14}

**Fig 3.5** J-V characteristics of experimental [9] and simulated GaAs-p-i-n SC.**Table 6** Experimental and simulated outputs.

Device	$V_{oc}(mV)$	$J_{sc}(mA/cm^2)$	$FF(\%)$	$\eta(\%)$
Experimental [9]	861.40	18.80	64.20	10.40
Simulation	800.50	18.94	78.66	11.92

A good agreement is remarked between experimental and simulated results. Then next, we have to take into account these defects in the basic structure (matrix structure) of the QDSC.

Now, 10-layers of QDs are embedded in intrinsic region of the previous solar cell with only intrinsic original defects. The result on J-V and outputs is presented, respectively, in **Fig 3.6** and **Table 7**.

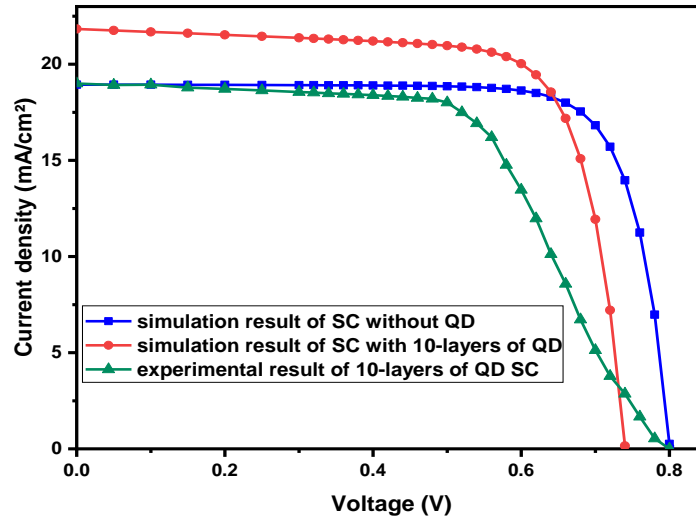


Fig 3.6 J-V characteristics of solar cell, with and without QD, in presence of original defects compared to experimental J-V of 10-layers QDSC.

Table 7 Outputs of solar cell with and without QD taking into account original defects.

Device	$V_{oc}(mV)$	$J_{sc}(mA/cm^2)$	$FF\%$	$\eta\%$
Classical	800.50	18.94	78.66	11.92
With QD	740.30	21.90	74.60	12.10
Experimental QDSC	792.30	19.00	60.20	9.1

Despite that we have taken into account the presence of defects, the deviation between experimental and simulated QDSC is significantly important. This is probably due to a further defects resulting from InAs/GaAs QDs implantation.

The resulted defects from the QDs are classified into two types, discrete levels and tail states. The first ones resulting from the arsenic atom excess or indium vacancies near the QD and are considered as electron traps [10].

The second type results from disordered structure. Since, the self-assembled InAs/GaAs quantum dots create perturbation to the GaAs lattice periodicity. The strained lattice forms a valence band tail states (VBTs) related to the existence of strain-induced dislocations. These dislocations are not located only in the intrinsic region but they move along the full structure including emitter and base [11-12-13-14]. The electron trap levels and VBTs parameters are given, respectively, in **Table 8** and **9**.

Table 8 Properties of electron traps induced by QDs [10].

Discrete defects	Type	Trap energy (meV)	Capture Cross section (cm ²)
Q1	Electron trap	127	3.1×10^{-15}
Q2	Electron trap	156	1.6×10^{-15}

Table 9 Properties of valence band tail states[11].

Continuous defect	Urbach energy (meV)	$N_{TD} \text{ cm}^{-3}$
Q3	50	1×10^{18}

The obtained J-V curve is shown and compared to experimental measurement in **Fig 3.7** and **Table 10**.

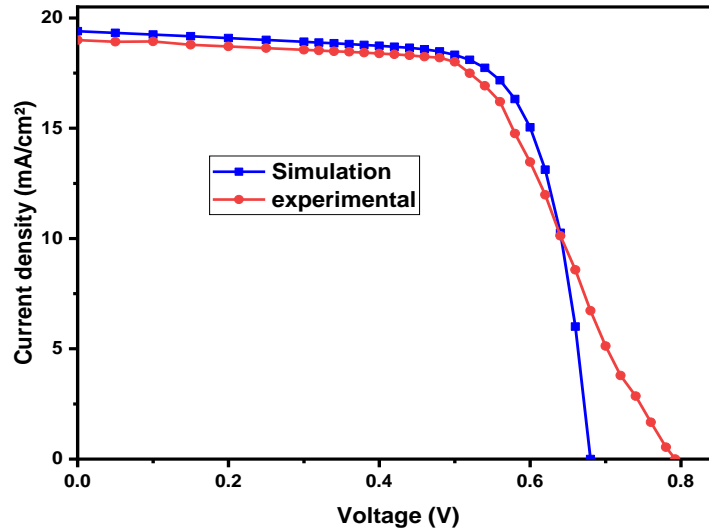


Fig 3.7 J-V characteristics of experimental and simulated QDSC with further defects related to QDs.

Table 10 Outputs of experimental and simulated QDSC with further defects related to QDs.

Device	$V_{oc}(mV)$	$J_{sc}(mA/cm^2)$	$FF\%$	$\eta\%$
experimental[9]	792.30	19.00	60.20	9.10
Simulation	680.00	19.40	73.00	9.60

We can observe a good agreement between simulation and experimental measurements. However, simulation gives better FF (which reflect the cell quality) and lower V_{oc} . The experimental measurement with a V_{oc} that induces an unusual shape of the curve (lower FF) indicates that there are another possible causes. It seems that the considered tunneling and thermionic emission transport models are not enough to reproduce the correct V_{oc} compromise between the higher band gap and the lower band gap energies.

Among the further possible process is the presence of tunneling through traps [15]. Or probably because the QDs in practice are doped therefore the experimental value of V_{oc} is greater than the simulation one.

To improve more the agreement with the experimental J-V curve, we chose a random QD distribution which is presented in **Fig.3.8**. The obtained result is shown in **Fig 3.9** and **Table 11**.

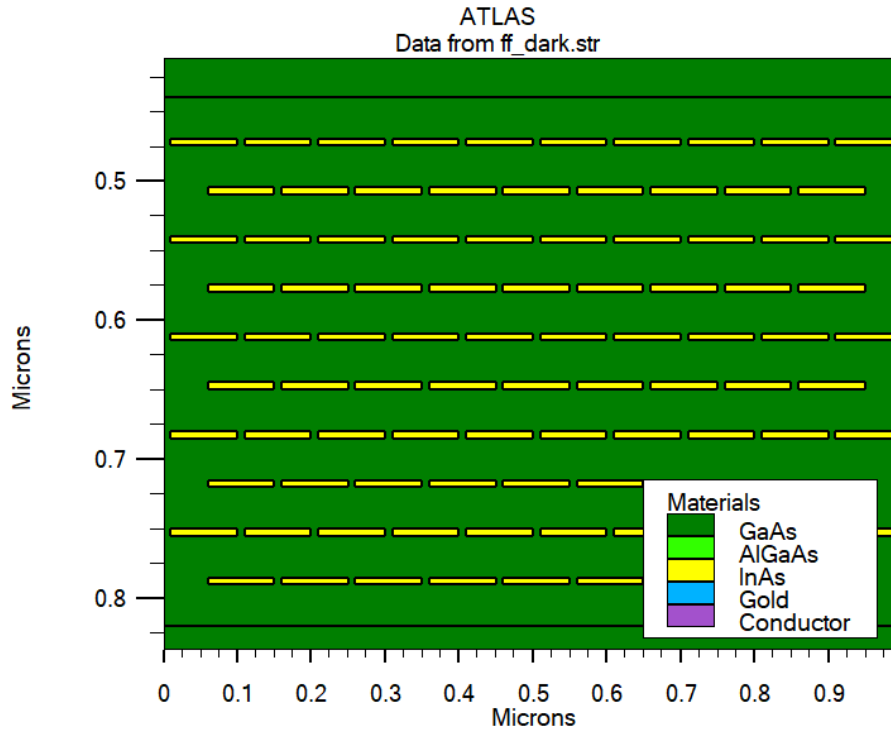


Fig 3.8 Quasi-random distribution of QD.

J_{sc} becomes identical to the experimental value while, unluckily, V_{oc} exhibits further slight decrease.

Table 11 Quasi-random distribution of QDs effect on outputs.

Device	$V_{oc}(mV)$	$J_{sc}(mA/cm^2)$	$FF\%$	$\eta\%$
Experimental	792.30	19.00	60.20	9.10
Simulation	677.42	18.99	73.60	9.40

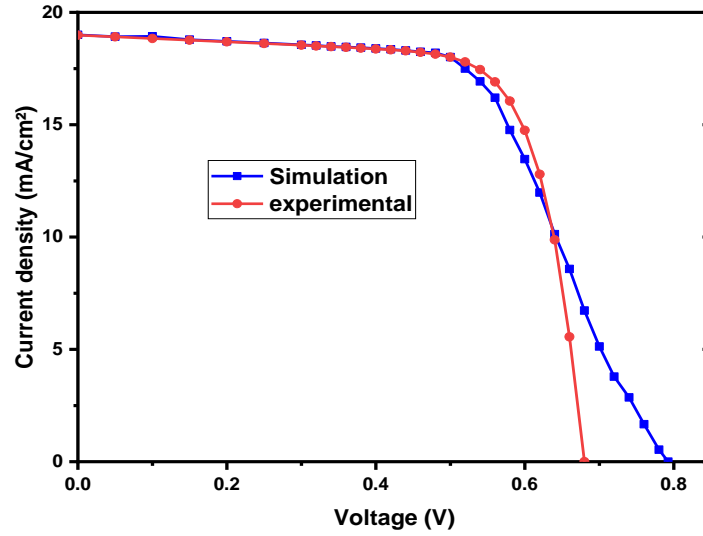


Fig 3.9 Effect of quasi-random distribution of QDs on J-V

3.4 Optimization of the InAs/GaAs QDSC

3.4.1 Effect of doping QDs on the real J-V characteristic

In this section, we study the effect of doping the QD on the real J-V characteristics.

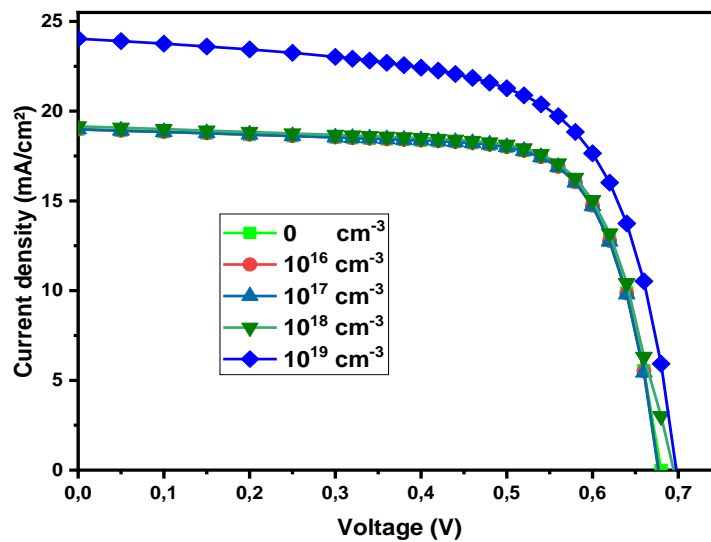


Fig 3.10 Effect of QDs doping on J-V characteristic of QDSC.

The effect is presented in **Fig 3.10** and **Table 12**. From results, unlike to the ideal QDSC, the cell is strongly affected by the doping density increase. It seems that doping is more efficient when defects are present and helps to neutralize them [5].

Table 12 Effect of QD doping on outputs.

Doping(cm^{-3})	V_{oc} (mV)	J_{sc} (mA/cm ²)	FF %	η %
0	677.42	18.99	73.60	9.40
1×10^{16}	677.41	18.99	73.60	9.46
1×10^{17}	676.89	19.00	73.58	9.45
1×10^{18}	690.00	19.20	68.80	9.60
1×10^{19}	697.76	24.04	65.83	11.04

3.4.2 Effect of using GaP layers in intrinsic region

Bailey et al suggest the use of GaP strain-balancing layer in intrinsic region as shown in **Fig 3.11** [6]. The results are shown in **Fig 3.12** and **Table 13**.

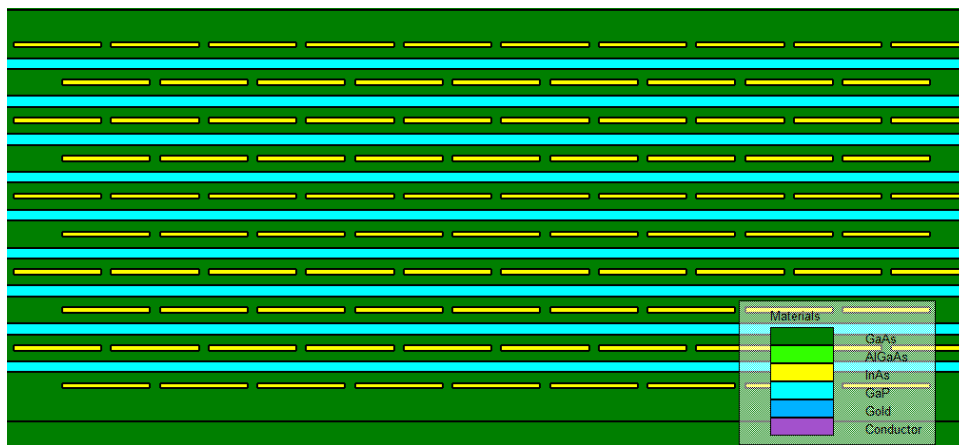


Fig 3.11 GaP strain-balancing layers in QD solar cell.

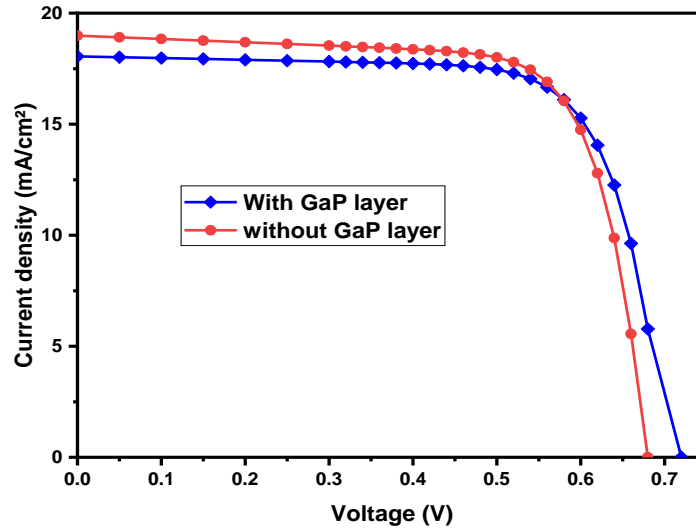


Fig 3.12 J-V characteristics of QDSC with GaP layers

Table 13 Outputs using GaP layers in the intrinsic region

Device	V_{oc} (mV)	J_{sc} (mA/cm ²)	FF %	η %
Without GaP layer	677.42	18.99	73.60	9.40
With GaP layer	700.30	18.05	73.87	9.34

The GaP has a band energy of 2.25 eV and this gives an increase in V_{oc} in agreement with experimental works, which used this layer to improve V_{oc} [6-7].

3.4.3 Effect of number of QDs layers

In the ideal case, the increase of QD layers has improved continuously the outputs of the solar cell. Now, we want to check this effect in the real structure especially since in experiment it is not evident that the increase of the QD layers improves J_{sc} [14].

The obtained results are presented in Fig 3.13, Table 14 and Fig 3.14.

J_{sc} improves with the increase of the number of layers until only 2-layers. The increase is related to the absorption of solar cell while the decrease starting from 3-layers is controlled

by the free carrier lifetime (diffusion length). An increase in V_{oc} from 1 to 2-layers of QD related also to the free carrier lifetime. The same improvement is noticed for the cell efficiency for 2-layers QD.

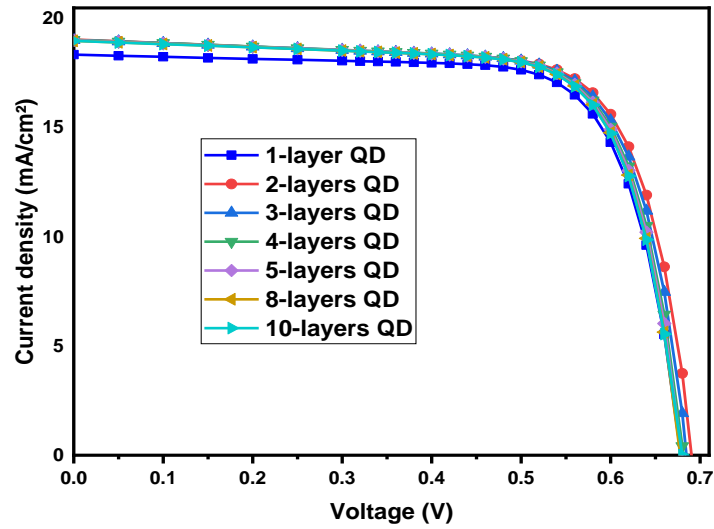


Fig 3-13 J-V characteristics of real QDSC with different QD layers number

Table 14 Effect of QD layers on outputs.

Number of layers	$V_{oc}(mV)$	$J_{sc}(mA/cm^2)$	$FF\%$	$\eta\%$
1	678.56	18.36	74.24	9.25
2	690.36	19.06	73.49	9.70
3	684.65	19.03	73.71	9.60
4	680.94	19.03	73.67	9.55
5	679.50	19.02	73.64	9.52
8	677.80	19	73.61	9.48
10	677.42	18.99	73.60	9.40

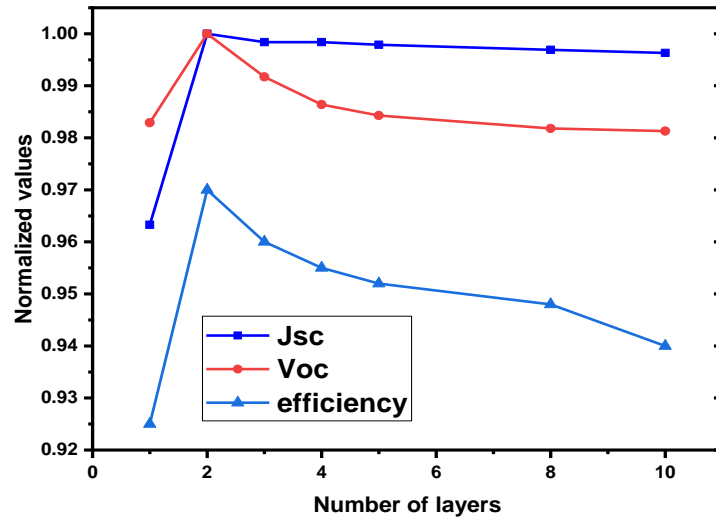


Fig 3-14 Effect the number of QD layers on J_{sc} , V_{oc} and efficiency.

After the full study, combining the better doping density with the better QD layer number; the highest expected efficiency is 11.29%, for 2-layers of QDs with doping of $1 \times 10^{19} \text{cm}^{-3}$ as shown in **Table 15**.

Table 15 highest expected efficiency for QDSC

Device	$V_{oc}(mV)$	$J_{sc}(mA/cm^2)$	$FF\%$	$\eta\%$
Optimal SC	734.50	20.69	74.26	11.29

3.5 Conclusion

QDSC was simulated by SILVACO-ATLAS. For the ideal case, it was found that the increase of QDs layers has improved monolithically the solar cell performance while doping has no significant effect. In the ideal case, the best obtained efficiency was 43.05 %. However, this is not in agreement with experimental works. To reproduce the experimental QDSC J-V, native defects with discrete levels and additional defects resulting from InAs/GaAs QDs layers were taken into account; the electron traps levels result from the arsenic atom excess or indium vacancies near the QDs and the valence tail states originate from the perturbation of lattice periodicity GaAs. The obtained efficiency in this condition was 9.4 % in agreement with experimental efficiency of 9.1%. Finally, this QDSC was improved through doping and the number of QDs layers. The optimum obtained efficiency was 11.29 % for 2-layers of QDs and a doping density of $1 \times 10^{19} \text{cm}^{-3}$.

References

- [1] U. Aeberhard, Simulation of nanostructure-based high-efficiency solar cells; challenges, existing approaches, and future directions, *IEEE Journal of Selected Topics in Quantum electronic* 19 (2013), 1-11.
- [2] A. Luque, A. Marti, A. J. Nozik, Solar cells based on quantum dots: multiple exciton generation and intermediate bands, *MRS bulletin* 32 (2007) 236-241.
- [3] F. Benyettou, A. Aissat, M. Djebari, J. Vilcot, Electrical properties of InAsP/Si quantum dot solar cell, *International Journal of Hydrogen Energy* 42 (2017), 19512-19517.
- [4] B. Dong, C. G. Bailey, A. Afanasev, M. Zaghloul, Modeling and simulation of InAs/GaAs quantum dot solar cell in SILVACO TCAD in: 2014 IEEE 40th Photovoltaic Specialist Conference (PVSC), IEEE, PP. 0476-0478.
- [5] X. Yang, K. Wang, Y. Gu, H. Ni, X. Wang, Z. Wang, Improved efficiency of InAs/GaAs quantum dots solar cell by Si-doping, *Solar Energy Materials and Solar cells* 113 (2013) 144-147.
- [6] C. G. Bailey, D. V. Forbes, S. J. Polly, Z. S. Bittner, Y. Dai, C. Mackos, R. P. Raffaele, S. M. Hubbard, Open-Circuit Voltage improvement of InAs/GaAs quantum dots solar cells using reduced InAs coverage, *IEEE, Journal of Photovoltaics* 2 (2012), 269-275.
- [7] S. Hubbard, C. Cress, C. Bailey, R. Raffaele, S. Bailey, D. Wilt, Effect of strain compensation on quantum dot enhanced GaAs solar cells, *Applied Physics Letters* 92 (2008) 123512.
- [8] J. C. Bourgoin, H. J. von Bardeleben, and D. Stiévenard, Native defects in gallium arsenide, *J. Appl. Phys.* 64, R65 (1988).
- [9] J. Zribi, B. Ilahi, B. Paquette, A. Jaouad, O. Theriault, K. Hinzer, R. Cheriton, G. Patriarche, S. Fafard, V. Aimez, et al, Effect of dot-height truncation on the device performance of multilayer InAs/GaAs quantum dot solar cells, *IEEE Journal of Photovoltaics* 6 (2016) 584-589.

- [10] C. Park, H. Kim, Y. Lee, D. Kim, T. Kang, C. Hong, H. Cho, M. Kim, Deep level defects of InAs quantum dots grown on GaAs by molecular beam epitaxy. *Journal of Crystal growth* 227 (2001) 1057-1061.
- [11] T. Li, M. Dagenais, Urbach tail in intermediate band InAs/GaAs quantum dot solar cells, in:2014, IEEE 40th Photovoltaic Specialist Conference (PVSC), IEEE, PP. 3622-3625.
- [12] Ted Thorbeck, Neil M. Zimmerman “Formation of strain-induced quantum dots in gated semiconductors nanostructures”, *Applied physics Letters*, 2015, 087107
- [13] S. Gaan, G. He, R. M. Feenstra, J. Walker, E. Towe, Electronic states of InAs/GaAs quantum dots by scanning tunneling Spectroscopy, *Applied Physics Letters* 97 (2010) 123110.
- [14] A. Marti, N. Lopez, E. Antolin, E. Canovas, A. Luque, C. Stanley, C. Farmer, P. Diaz, Emitter degradation in quantum dot intermediate band solar cells, *Applied Physics Letters* 90 (2007) 233510.
- [15] S. Willis, J. Dimmock, F. Tutu, H. Liu, M. Peinado, H. Assender, A. Watt, I. Sellers, Defect mediated extraction in InAs/GaAs quantum dot solar cells, *Solar Energy Materials and solar cells* 102 (2012), 142-147.

Conclusion

In this dissertation, InAs/GaAs multi-quantum well and quantum dots solar cells were simulated by MATLAB and Silvaco Atlas, respectively.

First, a p-i-n InAs/GaAs multi-quantum well solar cell was simulated by MATLAB. In addition to Drift-Diffusion model, the Schrödinger equation is also included. We found an increase in efficiency from 16.78% to 18.52%. This increase due to the increase in short circuit current.

Second, a p-i-n InAs/GaAs quantum dots solar cell was simulated by Silvaco Atlas. The quantum dots are inserted inside intrinsic region. This structure based on a real fabricated solar cell. The simulation was divided onto ideal case and real case.

In the ideal case, it was found that the increase of QDs layers has improved monolithically the solar cell performance while doping has no significant effect. In the ideal case, the best obtained efficiency was 43.05 % for 10-layers of QDs. However, this is not in agreement with experimental works. To reproduce the experimental QDSC J-V native defects with discrete levels and additional defects resulting from InAs/GaAs QDs layers were taken into account; the electron traps levels result from the arsenic atom excess or indium vacancies near the QDs and the valence tail states originate from the perturbation of lattice periodicity GaAs. The obtained efficiency in this condition was 9.4 % in agreement with experimental efficiency of 9.1%. Finally, this QDSC was improved through doping and the number of QDs layers. The optimum obtained efficiency was 11.29 % for 2-layers of QDs and a doping density of $1 \times 10^{19} \text{ cm}^{-3}$.

Finally, as all discussed above, all the simulation results in this dissertation have shown accuracy when comparing with experimental work. This dissertation helps build correct, complete models for both multi-quantum well solar cells and quantum dots solar cells.

These obtained results can help to develop solar cells with high-efficiency, and why not help to develop new technology for this type of solar cell because the technology of quantum dots in our view did not developed enough to manufacture quantum dots solar cell with high efficiency.

Abstract :

In this dissertation InAs/GaAs quantum solar cells is studied. First with a quantum well conception (QWSCs) and secondly with quantum dots (QDSCs).

For the InAs/GaAs QW, we used MATLAB to develop our own program to solve consistently the classical drift-diffusion model with Schrödinger-Poisson model. The QWSC provided a cell efficiency of 18.52% compared with 16.78% for the classical one.

The InAs/GaAs QDSC was studied using Silvaco Atlas simulator. The study is divided into two parts: ideal and real case. The effects of the number of quantum dots (QDs) layers and the doping of QDs on electrical properties of QDSC are investigated. A highest efficiency of 43.05 % was obtained in the ideal case. However experimental works have reported a conversion efficiency of 9.1%. Taking into account the presence of discrete electron traps and valence band tail, we were able to obtain a cell efficiency of 9.4% in agreement with experimental reports. In addition, it was possible to improve the cell efficiency to 11.29% by optimizing the number and the doping of QDs layers, to 2-layers and $1 \times 10^{19} cm^{-3}$, respectively.

ملخص:

في هذه المذكرة تمت دراسة خلية شمسية كمومية (InAs/GaAs). أولاً في حالة الأبار الكمومية وثانياً في حالة النقاط الكمومية.

في حالة الأبار الكمومية، استعملنا MATLAB لتطوير برنامجنا الخاص لحل نموذج جر-انتشار مع نموذج شرودنجر-بواسون. قدمت الخلية الشمسية بالأبار الكمومية مردود 18.52% بالمقارنة بـ 16.78% في حالة الخلية الشمسية الكلاسيكية.

تمت دراسة خلية شمسية بالنقاط الكمومية (InAs/GaAs) باستخدام برنامج محاكاة يدعى Silvaco Atlas. وتنقسم الدراسة إلى قسمين: حالة مثالية وحقيقية. تمت دراسة تأثير عدد طبقات النقاط الكمومية وتأثير تطعيم النقاط الكمومية على الخصائص الكهربائية للخلية الشمسية بالنقاط الكمومية. تم الحصول على أعلى مردود والذي وصل إلى 43.05 % في الحالة المثالية. في حين أنه قد وجد تجريباً مردود 9.1%. مع الأخذ في عين الاعتبار وجود فخاخ للإلكترونات وذبول العصابات، تمكنا من الحصول على كفاءة تقدر بـ 9.4% والتي تتفق مع النتيجة التجريبية. بالإضافة إلى ذلك، كان من الممكن تحسين مردود الخلية إلى 11.29% عن طريق تحسين عدد الطبقات و تطعيم النقاط الكمومية إلى طبقتين و $1 \times 10^{19} cm^{-3}$ على التوالي .